Atmos. Meas. Tech. Discuss., 5, 2959–3018, 2012
www.atmos-meas-tech-discuss.net/5/2959/2012/
doi:10.5194/amtd-5-2959-2012

Atmospheric Measurement Techniques Discussions

Level 1 algorithms for TANSO on GOSAT: processing and on-orbit calibrations

A. Kuze[1], H. Suto[1], K. Shiomi[1], T. Urabe[1], M. Nakajima[1], J. Yoshida[2], T. Kawashima[2], Y. Yamamoto[3], and F. Kataoka[4]

[1]Japan Aerospace Exploration Agency, Tsukuba-city, Ibaraki, Japan
[2]NEC Toshiba Space Systems, Ltd., Fuchu, Tokyo, Japan
[3]NEC Informatec Systems, Ltd., Kawasaki-City, Kanagawa Japan
[4]Remote Sensing Technology Center of Japan, Tsukuba-city, Ibaraki, Japan

Received: 5 February 2012 – Accepted: 9 April 2012 – Published: 24 April 2012

Correspondence to: A. Kuze (kuze.akihiko@jaxa.jp)

Published by Copernicus Publications on behalf of the European Geosciences Union.

Abstract

The Thermal And Near infrared Sensor for carbon Observation Fourier-Transform Spectrometer (TANSO-FTS) onboard the Greenhouse gases Observing SATellite (GOSAT)(nicknamed "Ibuki") has been providing global space-borne observations of carbon dioxide (CO_2) and methane (CH_4) since 2009. In this paper, first, the most recent operational Level 1 algorithms to produce the spectral radiance from the acquired interferogram are described. Second, we will describe the on-orbit characteristics and calibrations of TANSO-FTS. Overall functions and performances such as signal to noise ratio and spectral resolution are within design objectives. Correction methods of small on-orbit degradations and anomalies, which have been found since the launch are described. Lastly, calibrations of TANSO Cloud and Aerosol Imager (TANSO-CAI) are summarized. However, the Level 1B algorithms of TANSO-CAI are not mentioned, here in this paper.

1 Introduction

1.1 Overview

The Greenhouse gases Observing SATellite (GOSAT) was successfully launched into a sun-synchronous orbit on 23 January 2009 to monitor mainly global distributions of carbon dioxide (CO_2) and methane (CH_4). GOSAT carries two instruments, namely, the Thermal And Near infrared Sensor for carbon Observation Fourier-Transform Spectrometer (TANSO-FTS) and the Cloud and Aerosol Imager (TANSO-CAI). TANSO-FTS measures the reflected radiances in the oxygen (O_2) A band at 0.76 µm (Band 1) and in the weak and strong CO_2 bands at 1.6 µm (Band 2) and 2.0 µm (Band 3), and also the CH_4 bands at 1.67 µm (Band 2) with two orthogonal linear polarizations, designated "P" and "S", and the thermal radiation (Band 4). TANSO-CAI has four spectral bands, namely, 0.380 µm (Band 1), 0.674 µm (Band 2), 0.870 µm (Band 3), and 1.60 µm (Band

AMTD
5, 2959–3018, 2012

4) to extract clear soundings of the TANSO-FTS measurements and to provide cloud and aerosol optical properties.

GOSAT is a joint project of the Japan Aerospace Exploration Agency (JAXA), Ministry of the Environment (MOE) and the National Institute for Environmental Studies (NIES). JAXA is responsible for producing the Level 1A (raw interferogram) and the Level 1B (spectral radiance) products of TANSO-FTS and the Level 1A (raw digital number) product of TANSO-CAI, while NIES provides the Level 2 (CO_2 and CH_4 concentrations from each Level 1B spectra), the Level 3 (global distribution of CO_2 and CH_4 concentrations by interpolating the Level 2 products), and the Level 4 (net CO_2 sources and sinks) products of TANSO-FTS and the Levels 1B, 1B+, 2, and 3 products of TANSO-CAI. These products are provided in the Hierarchical Data Format 5 (HDF5) format except for the Level 4 product, which is saved in the Network Common Data Form (NetCDF) format and in text. The data level, product, format, and responsible institute are summarized in Table 1. All signals (Level 0) transmitted from the GOSAT satellite are received at KSAT, Norway and Earth Observation Center (EOC), Japan and transmitted to Tsukuba Space Center (TKSC), Japan. Thereafter, the TANSO-FTS Levels 1A and 1B data and the TANSO-CAI Level 1A data are produced at TKSC. Usually the Level 1 data is transferred to NIES and other users such as the National Aeronautics and Space Administration (NASA) in the United States and the European Space Agency (ESA) within 5 h after the initial observation on orbit. The Level 1B data together with all the necessary calibration and correction data and the higher data products produced in NIES are available at the NIES GOSAT User Interface Gateway (GUIG). The camera (CAM) data is not processed as the Level 1 product because the camera was originally installed to check alignment onboard. We describe the data processing algorithms of the TANSO Levels 1A and 1B, which are JAXA's responsibility. The details of the Level 2 algorithms are described in Yoshida et al. (2010) for TANSO-FTS short wave infra-red (SWIR) bands, Saitoh et al. (2009) for thermal infra-red (TIR) band and Ishida et al. (2009, 2011) for TANSO-CAI.

AMTD
5, 2959–3018, 2012

1.2 TANSO instruments

The schematics of the TANSO-FTS and CAI optics modules are illustrated in Fig. 1. TANSO-FTS has many functions and operational modes. The two axes optical mirror pointing mechanism has pointing and image motion compensation functions and the views of the earth and the calibration sources. In nominal observation mode, the pointing mechanism views the grid points. In the sun-glint observation and special target modes, the optical mirror pointing mechanism views the specular reflection points over the ocean and requested observation points, respectively. The FTS mechanism also has an actuator rotary voice-coil to create the optical path difference (OPD) of the interferometer. The performance of these two mechanisms on orbit has to be carefully characterized and the performance is described in Sects. 2.2.3 and 3.4. TANSO-CAI is a much simpler instrument. It has no mechanical moving parts and no onboard calibrator. It has a wide swath of 910 km and acquires the global image in 3 days. The spectral and geometrical performance of TANSO-CAI on orbit can be assumed to be stable. During the day time both SWIR and TIR of TANSO-FTS and TANSO-CAI data are acquired and during the night time only TANSO-FTS TIR data is acquired. Overall the radiometric responses of both TANSO-FTS and CAI are the combination of the optical efficiency, detector response, and the amplitude of the analogue circuits. On orbit the response change with time has been monitored for three years and characterized in this paper. More details related to each instrument design, pre-launch hardware performances, and on-orbit operation were described in Kuze et al. (2009).

1.3 GOSAT operation

The function and performance of all systems were verified to meet operating standards during the initial three-month check-out phase after the launch (mid-January and mid-April, 2009). In the second three-month phase (May–July, 2009), the initial calibration was required. During this period, the first vicarious campaign was performed and responses of TANSO-FTS and CAI were calibrated (Kuze et al., 2011a). Nominal

AMTD
5, 2959–3018, 2012

operation phase started in July 2009. More than three years have passed since the launch, and the overall functions and performances are within design objectives. All the measured spectral radiance of the TANSO-FTS SWIR and TIR bands and column-averaged dry air mole fractions (the Level 2 product) of CO_2 and CH_4 (X_{CO_2} and X_{CH_4}, respectively) retrieved from the SWIR bands are currently available to the public from NIES. Several different groups also have derived X_{CO_2} and X_{CO_2} other than the GOSAT standard Level 2 product (Butz et al., 2011; Parker et al., 2011; O'Dell et al., 2012; Crisp et al., 2012). In addition to the greenhouse gases, chlorophyll fluorescence has been measured first time from space using high-spectral-resolution Fraunhofer line spectra by Joiner et al. (2011, 2012), Frankenberg et al. (2011a, b), and Gunter et al. (2012).

GOSAT has a 3-day revisit orbit cycle and a 12-day operation cycle. There are three operation patterns on how to insert the target observations to the nominal grid observations. These are pattern A, i.e. neither sun glint nor target observations but limited validation sites observations; pattern B, i.e. sun glint over the ocean in the low latitudes in the neighborhood of the sun's declination and target observations requested by the registered researchers adopted to research announcements (RA); and pattern C, i.e. sun glint and limited target observations for validation sites only. Each pattern continues for three days in the repeated order of the patterns is A, B, C, and B. The detailed operation modifications in chronological order were described in Kuze et al. (2011b).

Several anomalies were found in TANSO-FTS on-orbit operation and the operation was modified to avoid the performance degradation (Kuze et al., 2011c). One of the major anomalies is the zero path difference (ZPD) shift, which degrades the spectral resolution and must be corrected. ZPD is the center of the interferogram. The FTS-mechanism controller counts laser fringes for uniform-speed scans within the maximum optical path difference (MOPD) and then drives the FTS-mechanism scan-arm to motion. Turnaround is a loss of observation time, which needs to be minimized. During turnarounds, both FTS-mechanism and optical mirror pointing mechanism are activated simultaneously. A combination of micro-vibrations caused by the mirror pointing motion, a slower-speed scan in an electro-magnetic-noise environment, along with

AMTD
5, 2959–3018, 2012

degradation of laser-detection level occasionally caused the controller of the FTS-mechanism to miss counting the laser fringes at the turnaround position and then the ZPD position shifts gradually. We now periodically reset the ZPD position by uploading the command from the ground. The shifted fringe number is being recorded in the Level 1B product.

The other major anomaly is a pointing bias after "an imperfect settling down" of the optical mirror pointing mechanism, which is due to the two following possible reasons. One is the bias of the angular resolver (an angular position sensor) data and the other one is the insufficient electrical power to properly drive the along track (AT) motor. Besides, within the AT motion range, there are a few "dead bands", where the AT motion becomes unstable or even occasionally settles down in the imperfect positions. The two of the original five cross-track points shown in Fig. 2a are close to dead-band angles and they have large biases: in some cases they can be detected by the resolver and then they can be geometrically corrected. Instead of an ideal grid, an M shape pattern was introduced between 26 June 2009 and 31 July 2010, to avoid the dead-band areas and to minimize the pointing anomalies as illustrated in Fig. 2b. The exact pointing locations of the M shape can be retrieved in the Level 1B geolocation data. On the other hand, three cross-track points as shown in Fig. 2c does not use dead-band area. Therefore, 3-point cross-track scan mode has been conducted afterwards. The trend of the bias and the geometric collection method using camera data are to be described later.

Between the launch and July 2010, interferograms had been acquired every 4.45 s (4 s for interferogram acquisition and 0.45 s for turnaround) for the 5-points in the cross-track (CT) direction, which resulted in 150 km spacing between grid observations and a total of 56 000 points globally every three days. Since August 2010, the sun glint observation uses the image motion compensation (IMC) to minimize the input intensity fluctuation and to reduce the cloud contamination. Since then, the grid observation patterns also have changed from 5-point cross-track scan mode to 3-point cross-track

AMTD
5, 2959–3018, 2012

scan mode with 260 km spacing. The longer turnaround time of 0.6 s probably decrease the ZPD shift speed.

Thus, so far, owing much to the careful satellite and sensors operation from the ground, the overall function of TANSO-FTS has been stable. The radiometric, geometric, spectrometric, and polarimetric performances have been good owing to the modification of the Level 1 algorithm and proper calibrations. The Level 1 algorithm and processing flows to create spectral radiance from acquired interferogram are described in Sect. 2. In Sect. 3, the performance characterization of on-orbit, onboard and vicarious calibrations are being presented. Lastly, TANSO-CAI characterization and calibration are being described in Sect. 4.

2 TANSO-FTS Level 1 algorithm

In this section, the most recent TANSO-FTS Level 1 algorithm is described. The name of this version has not been determined yet. The algorithm has been updated several times since the launch. The version in chronological order was described in Kuze et al. (2011b).

All the raw interferogram (digital number) are being saved as the Level 1A data. The payload correction data from the satellite bus and telemetry data of TANSO-FTS are added in both Levels 1A and 1B products together with the measured data. These data include the time stamp, the satellite and sun position, the geolocation, the AT and CT angles of the optical mirror pointing mechanism, the detector temperature, the blackbody (BB) temperature, and gain level, all of which are necessary for the data processing and analysis. The time stamp in data shows the start of the interferogram acquisition, which is equal to the end of the FTS mechanism turn around. The satellite position is interpolated by using the payload correction data, which is transmitted from the satellite every second. The AT, CT, solar angle, and the geometry information are acquired at the start of the interferogram acquisition.

AMTD
5, 2959–3018, 2012

2.1 Procedures

Interferograms of each band (two linear polarizations of bands 1, 2, and 3 and scalar band 4) are processed independently. TANSO-FTS bands 1, 2 and 3 (SWIR) are processed as follows:

Step S1: Saturation detection

Step S2: Correction of spike noise detection caused by cosmic rays onto the detector

Step S3: Scan speed instability correction (applied for Band 1 medium gain only)

Step S4: Low frequency component correction (bands 2 and 3 only)

Step S5: Laser sampling interval non-uniformity correction

Step S6: Direct current (DC) extraction and ZPD detection

Step S7: Inverse Fast Fourier transform (IFFT)

Step S8: Phase correction

Step S9: Analogue circuit non-linearity correction.

TANSO-FTS Band 4 (TIR) is processed as follows:

Step T1: Correction of spike noises caused by cosmic rays onto the detector

Step T2: Non-linearity correction of the Band 4 photo conductive (PC) – mercury cadmium telluride (MCT) detector

Step T3: ZPD detection and IFFT

AMTD
5, 2959–3018, 2012

Step T4: Complex radiometric calibration and deep space (DS) view obscuration correction

Step T5: Polarization correction of the pointing mirror.

A detailed flow diagram is shown in Fig. 3 and each process is explained in the following sub-sections.

2.2 Corrections

2.2.1 Saturation and spike noise detection and correction (Steps S1, S2, and T1)

First, saturated interferograms are screened. Saturation at the ZPD of interferograms occurs mainly in the pre-amplifier and analog-to-digital converter (ADC). As the outputs of the pre-amplifiers are phase delayed, the saturation at the input cannot be explicitly detected. There is the possibility of saturation when the interferogram reconstructed from low-frequency components is negative at ZPD or the digital number is over 65 400. Subsequently, the interferograms that have jumped due to the gain change and have fluctuations are being screened. The fluctuation on the interferogram is generated by the optical mirror pointing mechanism's unstable settling down over the non-uniform targets. Even though there have been no cosmic rays detected since the launch, the high energy particles also create spikes. These unexpected fluctuation and spikes of the interferogram are being screened and a quality flag is attached to the Level 1B data. The fluctuation is corrected in the low-frequency component correction process described in Sect. 2.2.4 and spikes are removed and filled with an estimated DC signal, which is the average of the interferogram levels acquired before and after the spike.

2.2.2 Digitization and its non-linearity

Non-linearity of the raw interferogram readout should be corrected. There are three blocks in analogue electronics: namely the detector, analogue circuit, and ADC. Si detector of bands 1 and InGaAs detectors of bands 2 and 3 can be considered adequately

AMTD
5, 2959–3018, 2012

linear. The Band 4 PC-MCT detector has non-linearity, and its correction method is described in a later Sect. 2.2.7. The analogue circuit consists of the current-to-voltage converter, gain amplifier, and electric filters: the characteristics and correction are described in the Sect. 2.2.6.

FTS has a wide dynamic range and the same type of 16-bit ADCs are used for all bands. As it is not realistic to fine-tune the electronics gain for each interferogram, TANSO-FTS uses only two gain levels: high and medium. Therefore, when the surface albedo is low, the dynamic range of the interferogram is not optimized and the number of the bits used is limited. If the random noise is small, a low number of digitization bit creates systematic errors, which are difficult to correct. In addition, ADC itself has non-linearity. ADC non-linearity can be characterized by the differential non-linearity (DNL) and the integral non-linearity (INL). A DNL larger than 1 bit becomes missing code. By measuring DNL bit by bit, the INL of the entire dynamic range can be characterized. Figure 4 shows the INL correction value retrieved from the measured data using the TANSO-FTS engineering model. Non-linearity produces spectral artifact, which varies with the intensity level of the input flux. The 16-bit ADCs used in TANSO-FTS have the largest non-linearity at the center of the dynamic range (the first bit that determines the center word). Band 1 is alternating current (AC) sampled and the center bit is frequently used as OPD becomes larger. Although INL of the entire dynamic range has been characterized, it is still very difficult to correct the ADC-NL of low level AC sampled interferogram. When the input radiance is weak, the digitized interferogram at larger OPD uses the center word frequently. Once ADC-NL is corrected, the corrected spectra have systematic bias. The former version of V130.130 had tried to correct the ADC non-linearity. Particularly in the case of low input cases, the Level 1B products had large artifacts. Therefore, the most recent version does not correct the ADC non-linearity. In the case of very low input, the Level 1B data of Band 1 have the possible small bias.

AMTD
5, 2959–3018, 2012

2.2.3 Correction of scan speed instability (Step S3)

The phase delay mismatch between the metrology laser electronics and science channel degrades the robustness to the scan speed instability and then creates artifact spectra. Only the medium gain of Band 1, which we use over high reflectance regions such as the Sahara, Arabic and Australian deserts and solar calibration, has a significant delay mismatch: its amplifier circuit has a different group delay between high and medium gains and the delay is optimized only for high gain. When speed instability is large, the Band 1 interferogram with the medium gain is not sampled with the equal interval. In the worst case, the sampling interval changes by about ±0.6 % and the spectral radiance changes by ±1.5 %. The speed instability is caused by a combination of two sinusoidal micro-vibration sources, namely, a 244 Hz from the satellite attitude control's Earth sensor and the 325.5 Hz resonant frequency of the FTS mechanism. These additional modulations to the interferogram can be corrected by retrieving amplitudes and phases of those two sinusoidal micro vibrations for each interferogram acquired with medium gain. Every time each interferogram is processed, these four parameters are being estimated to minimize the out-of-the-band artifact spectra. The interferogram is then interpolated at the expected sampling positions but at the cost of additional computation resources in the ground data processing (Simon, 2008; Suto et al., 2010). After applying the correction from Version 110.110, the standard deviation of the Band 1 medium gain data has been significantly reduced to below noise level (Suto et al., 2011a).

2.2.4 Correction of the low-frequency component (Step S4)

The acquisition of both modulated and non-modulated portions of the interferogram of bands 2 and 3 is performed in order to check the data quality. TANSO-FTS has a fully redundant sampling system with two 1.31 µm distributed-feedback (DFB) lasers, which have much longer life time than a conventionally used HeNe laser. Interferogram has to be sampled shorter than half wavelength of the signal. The up-and-down

AMTD
5, 2959–3018, 2012

zero-crossings of laser-fringes are utilized for sampling triggers of 0.655 µm. The half of Band 1 wavelength of 0.76 µm is still shorter than the sampling wavelength and only modulated portion (AC) is acquired. We use aliased spectra of Band 1 with both electrical and optical band pass filters to eliminate ghost signals and minimize lower frequency aliasing noise. Band 4 is also AC sampled to reduce the non-modulated background radiation. On the other hand, DC sampling is applied to bands 2 and 3. By checking the DC sampled interferogram, the sudden jump of the level due to the pointing anomaly can be detected. DC sampled interferograms includes low-frequency components. Some interferograms contain the low-frequency components due to pointing jitter and optical vignetting. These frequencies are typically lower than 500 Hz and much lower than the scene signal modulation of the order of 10 KHz. They have independent amplitude and phase and can be extracted from the interferogram. We remove the low frequency-component by dividing interferogram created from the low frequency-components. This method is similar to the method applied to the FTSs of the Total Carbon Column Observing Network (TCCON) (Keppel-Aleks et al., 2007).

The largest contribution to the low-frequency components is the optical vignetting. The FTS mechanism is based on the double-pendulum scanning mechanism principal and its effective optical throughput becomes slightly lower as OPD increases due to vignetting. This apodization effect is corrected leaving the apodizations caused by the finite size of the field of the view and the detector alignment offset from the optical axis. All the bands 2 and 3 data have vignetting and are corrected.

The second contribution is scene flux fluctuation due to the constant satellite sinusoidal vibration motion. The typical frequency is about 10 Hz and the possible source is the satellite's reaction wheel. The last contribution is the pointing mirror fluctuation, which occurred irregularly. About 20 % of the total interferograms are affected by the fluctuation caused by the optical mirror pointing mechanism and have intensity modulation. We can detect these two fluctuations by checking the Band 2 interferogram. If the scene is perfectly spatially uniform, we cannot detect the optical mirror pointing

AMTD
5, 2959–3018, 2012

mechanism fluctuations. However, the spectra of the spatially uniform targets are not affected by these fluctuations.

2.2.5 Correction of sampling interval non-uniformity (Step S5)

The ideal interferogram of the scene flux is being acquired with equal sampling interval of the laser fringes within the entire OPD. The actual on-orbit interval changes very slightly with OPD, varying of 25 nm (peak to peak) from ZPD to maximum OPD. The change is not linear to OPD and the forward and backward scans of the FTS mechanism are different as shown in Fig. 5. The error caused by this non-uniformity is close to the noise level in the forward direction data but slightly larger in the backward scan data. The root cause is not well known, but it is probably caused by the laser optical misalignment, asymmetry of the FTS scan mechanism structure and its electronic control imperfection. As the difference is constant with time on orbit, this non-uniformity is corrected by resampling the interferogram.

2.2.6 Correction of Band 1 analogue circuit non-linearity (Step S9)

The high gain of Band 1 has high amplitude and its high-gain amplifier uses the Chebyshev filter with much sharper gain peak and cut-off to avoid aliasing of noise. Its gain is sensitive to the capacitance in the circuit, which is not constant with input voltage, temperature, and time. The Butterworth filters, which are used other than for the Band 1 high gain, have flat response and its capacitance change results in the cut-off position only. The non-linearity induced by the input-voltage change can be corrected using the 3rd order polynomial (Suto et al., 2011b). These coefficients are determined such that the out-of-the-band artifact spectra are minimized. The analogue circuit non-linearity is more complicated than that of the detector. It is the function of both the input voltage and the ZPD level. Thus, the non-linearity is corrected after the phase correction as indicated in Fig. 3. We have prepared the 3rd-order-coefficient tables as the function of the ZPD voltage. Temperature dependency might cause seasonal and orbit phase

AMTD
5, 2959–3018, 2012

changes and the time dependency might cause the long term changes. Band 1P has shown an especially larger change and these effects need a further investigation. We replaced the capacitor of the engineering model with the temperature compensated one in the laboratory on the ground and then the artifact spectra were removed. This test results indicate our correction algorithm works well.

2.2.7 Correction of TIR detector non-linearity (Step T2)

We use a PC-MCT detector, which has non-linearity for strong photon input in principle, only for Band 4. The non-linearity can be corrected using the 2nd order polynomial. Assuming that non-linearity characteristics do not change with time after the launch, the coefficients can be determined from the well-characterized large photon input data under the stable condition in a vacuum chamber prior to the launch. There are two ways to find the correction parameters. When the detector and its analogue electronics have non-linearity, the largest signal at ZPD is distorted and artifact low-frequency spectra are created. The correction coefficients are tuned such that interferogram created with low frequency components are flat near ZPD. The other method is to select the correction coefficients to fit the artifact shape at the edges of the band, i.e. 300–600 cm^{-1} and 2200–3500 cm^{-1}. The latter method is applied as it has larger sensitivity to determine the coefficients. They are fine-tuned such that corrected signals of the out-of-the-band region are flat. The non-linearity corrected data $V_{\mathrm{NLcorrected}}$ is calculated by the Eqs. (1) and (2) described below with measured raw AC components of the interferogram in voltage V_{AC} and DC voltage V_{DC}. V_{DC} is the average of DC samples, which are monitored at 38 points per interferogram. We subtract offset V_{DCoffset}, which has a gradual increase since the launch probably due to temperature change of the electric circuit. V_{DCoffset} is estimated from the DS view data and modeled as the function of the time since the launch.

$$V_{\mathrm{Pamp}} = -\left((V_{\mathrm{DC}} - V_{\mathrm{DCoffset}})/g_{\mathrm{DC}}\right) - V_{\mathrm{AC}}/g_{\mathrm{AC}}. \quad (1)$$

AMTD
5, 2959–3018, 2012

The gain factors g_{DC} and g_{AC} are 0.681 and 110.103, respectively.

$$V_{NLcorrected} = V_{Pamp} + a_{nlc} V_{Pamp}^2. \quad (2)$$

a_{nlc} is the non-linearity correction coefficient of 0.6056.

2.3 Inverse fast Fourier transform

2.3.1 ZPD detection and inverse fast Fourier transform (Steps S6, S7, and T3)

The ZPD position is determined by searching the center burst (peak) of the interferogram. The interferogram is then converted to the spectra with prime factor IFFT. ZPD position of the SWIR bands is searched in every interferogram processing assuming that the true ZPD is located near the center burst. On the other hand, for the TIR band, scene flux from the ground and atmosphere is close to the back ground radiation and it can be difficult to detect ZPD position when the input scene flux and radiation are balanced. Ideally, the ZPD position is calculated from the DS calibration when the background is dominant and we assume that it will not change between the DS calibrations, which typically occur in intervals of 25 min. However, when ZPD shift occurs, the ZPD has to be detected again such that the phase becomes spectrally flatter.

The number of laser fringes used for inverse Fourier transform is 76 336. As many data points are extracted as needed for data processing centered on ZPD. Based on the measured laser wavelength before the launch, the exact maximum OPD are 1309.742 nm × 76 336/2 = ±2.4995 cm for the primary laser source and 1309.688 nm × 76 336/2 = ±2.4994 cm for the secondary, which is slightly smaller than ±2.5 cm. Prime number-based combinations of 76 545 ($=3^7 \times 5 \times 7$) for bands 1, 2, and 3 and of 38 400 ($=2^9 \times 3 \times 5^2$) for Band 4 have been selected to save the computation time. A zero-filling should be carried out to fill the balance after ZPD shift correction is performed. The laser temperature is being controlled at a nominal value of 25° with variations smaller than the thermometer resolution of 0.7 mK. Therefore, laser wavelength has been very stable and OPD has been constant on orbit. When the ZPD position

AMTD
5, 2959–3018, 2012

is away from the center of an interferogram by more than 100, quality (warning) flag is set. If the ZPD position is away by more than 2000, interferogram data should be processed with an assumption that ZPD lies on the center of entire sampling points: after shifting ZPD, both ends of the interferogram data should be filled with zeros.

2.3.2 Phase correction (Step S8)

For SWIR data processing, electrical frequency characteristics, index-of-refraction wavelength dependency, and the ZPD position difference smaller than laser fringe make the phase differences. These phases have spectrally smooth structures. The degree of the phase can be retrieved from the ratio of the imaginary spectra to the real one. The phase is corrected such that imaginary spectra become noise level. At strong absorbed lines, it is difficult to distinguish the imaginary spectra from the noise. If we correct the phase of fully absorbed lines with high spectral resolution, sometimes the phase is over corrected. Imaginary part become much lower than noise level and the artificial part is created. Therefore the moderate spectral resolution of the phase retrieval, which is much wider than single absorption lines, has to be selected by extracting the portion near ZPD and filling zero into both sides of the interferogram. For TIR data processing, complex radiometric calibration is applied and phase is simultaneously corrected.

2.4 SWIR Level 1 B product

The real part of the complex spectra is the measured signal while the imaginary part represents the noise level of the measurement. The raw spectra is used to estimate signal-to-noise ratio (SNR) levels. The unit is output voltage per wavenumber (V cm). Subsequently, the spectra data with both real and imaginary parts are stored as the Level 1B data before converting to the spectral radiance. In addition, if degradation of the instrument optical efficiency or detector response is detected, we can update the radiance conversion factor without changing the Level 1B product. Response degradation

AMTD
5, 2959–3018, 2012

is discussed in the later Sect. 3.1. Low-frequency components are also stored as they include information on pointing fluctuations, target scene changes, and micro vibrations.

2.5 Complex radiometric calibration and corrections for TIR (Steps T4 and T5)

DS is a very cold target with a temperature of 3 K and its view data are equivalent to that of the background radiation from the TANSO-FTS optics. BB is used as the higher temperature standard. TIR spectral radiance is calibrated with these two on-orbit ideal sources without using pre-launch calibration. In addition to the detector non-linearity correction, two more fine corrections described below are needed: DS view obscuration and polarization.

Since both DS and BB calibrations, consisting of 2 sets of forward and backward data of a total of 8 interferograms, are scheduled frequently (4 times per orbit), on-orbit optical efficiency degradation does not affect the radiometric accuracy. Spectral radiances after the complex calibration from DS and BB spectra as expressed in Eq. (3) are provided as the Level 1B data. The forward and backward scan spectra are calibrated independently using better one set of forward and backward DS and BB scan data out of two.

$$B_{\mathrm{obs}}(\nu) = \frac{S_{\mathrm{obs}}(\nu,d) - (S_{\mathrm{DS}}(\nu,d) - \Delta S_{\mathrm{DS}}(\nu,d))}{S_{\mathrm{BB}}(\nu,d) - (S_{\mathrm{DS}}(\nu,d) - \Delta S_{\mathrm{DS}}(\nu,d))} B_{\mathrm{BBeffective}}(\nu) \tag{3}$$

In the above equation, $S_{\mathrm{obs}}(\nu,d)$, $S_{\mathrm{DS}}(\nu,d)$, and $S_{\mathrm{BB}}(\nu,d)$ denote measured spectra of nadir observation, DS, and BB, respectively. The symbols ν and d are the wavenumber and scan direction of the FTS mechanism.

Due to the pointing bias described earlier, the DS view is estimated to be obstructed by 3 % of the entire scene flux with the inner surface of the DS view hood of an estimated temperature of 250 K. The DS view obscuration correction is described as

AMTD
5, 2959–3018, 2012

follows:

$$\Delta S_{DS} = \gamma \frac{B(T_{DShood})}{B(T_{BB})}(S_{BB} - S_{DS}), \quad (4)$$

where γ is the obstruction rate and T_{DShood} and T_{BB} are the temperature of the DS view hood and BB. $B(T)$ is the calculated spectral radiance of temperature of T. T_{DShood} is an estimated value and T_{BB} is the blackbody temperature monitored with the onboard temperature sensors.

The effective spectral radiance $B_{BBeffective}$ is calculated with the equation below.

$$B_{BBeffective} = \varepsilon B(T_{BB}) + (1 - \varepsilon)B(T_{background}). \quad (5)$$

In the most recent version, we use the emissivity ε of 1 assuming that the environment temperature $T_{background}$ is close to the blackbody temperature. More detailed correction by using measured emissivity, background-view factor from the blackbody and background temperature is to be applied in the future.

The pointing mirror is viewing DS and BS calibrations sources horizontally by rotating the mirror by about 90°, whereas the scene flux is acquired from nadir. The coating of the pointing mirror is optimized for SWIR and both the pointing mirror and the FTS optics have polarization sensitivity at TIR region. Lastly, the polarization effect is corrected by using the following relation between $B_{obscorrected}(\nu)$, B_{obs} and $B_{mirror}(\nu)$ in case of nadir looking.

$$B_{obscorrected}(\nu) = \frac{((p_2^2+q_2^2)(p_1^2+q_1^2)-(p_2^2-q_2^2)(p_1^2-q_1^2))}{((p_2^2+q_2^2)(p_1^2+q_1^2)+(p_2^2-q_2^2)(p_1^2-q_1^2))} B_{obs}(\nu) + \frac{2(p_2^2-q_2^2)(p_1^2-q_1^2)}{((p_2^2+q_2^2)(p_1^2+q_1^2)+(p_2^2-q_2^2)(p_1^2-q_1^2))} B_{mirror}(\nu) + \Delta B_{bg}(\nu), \quad (6)$$

where p_1^2 and q_1^2 are optical efficiencies of two linear polarizations of the pointing mirror and p_2^2 and q_2^2 are corresponded to the FTS mechanism and the aft-optics. $B_{mirror}(\nu)$ is

AMTD
5, 2959–3018, 2012

the radiation from the pointing mirror surface, which is estimated from the temperature telemetry data near the optical mirror pointing mechanism. $\Delta B_{bg}(\nu)$ is the background radiation change between BB and DS calibrations, which is estimated from the orbit phase temperature variation model. $B_{obscorrected}(\nu)$ is the final Level 1B TIR products. More general formula is described in Mueller matrix in Sect. 3.5.

2.6 Time data in Level 1B product

The time stamp of the telemetry data is the turnaround completion time $T_{TAT,}$ which corresponds to the start of interferogram acquisition. The interferogram near ZPD is the most informative and ZPD passing time is calculated using the following relationship:

$$T_{ZPD} = T_{TAT} + T_S \frac{X_{ZPD}}{76336}, \quad (7)$$

where T_S is the scan duration and X_{ZPD} is the ZPD position in the vicinity of the median of 1–76336.

3 TANSO-FTS on orbit characterization and calibrations

The overall radiometric and spectroscopic performances are good and they are well within design objectives. Figure 6 shows the measured CO_2 spectrum of the Level 1B V050.050 along with the modeled spectrum for the retrieval V01.10 and the residual difference (Yoshida et al., 2011). The residual is close to the noise level and the spectral resolution is as designed. In this section, the calibrations after the launch are described. The instrument model and the items, which need corrections are summarized in Tables 2 and 3, respectively. The calibration events in chronological order were described in Kuze et al. (2011b). The time dependent degradation of the TANSO-FTS throughput (response) can be cross-checked by the methods described in the following subsections.

AMTD
5, 2959–3018, 2012

3.1 Radiometric calibration and on-orbit degradation

There are several ways for TANSO-FTS to estimate the calibration accuracy and degradation on orbit. SWIR and TIR are calibrated, independently.

3.1.1 Pre-launch calibration

As described in detail in Kuze et al. (2009) and Sakuma et al. (2010), the TANSO radiometric response was calibrated before the launch by using integrating spheres. An example of the radiance conversion factor is shown in Fig. 7. TANSO-FTS has channeling in Band 2S, which is caused by the multiple reflections at the band separation optics and its magnitude is stable. As demonstrated in Fig. 7, a small oscillation feature of the conversion factor corrects channeling simultaneously and produces channeling-corrected spectral radiance. We use the pre-launch calibration results in the laboratory with integrating spheres. To correct atmospheric absorption in the laboratory and draw the envelope, we used the thermal vacuum chamber test results that are not affected by absorption. An absolute radiometric accuracy of better than ±5 % was achieved prior to launch in order to achieve the 1 ppm X_{CO_2} accuracy.

3.1.2 Vicarious calibration for SWIR

The first vicarious calibration was performed in the summer of 2009. The measurement campaign was conducted using a dry lake bed in Railroad Valley (RRV), Nevada, USA with the NASA Atmospheric CO_2 Observations from Space (ACOS) team (Kuze et al., 2011a). The spectral radiance was calibrated by comparing the satellite-measured radiances and simulated radiances at the top of the atmosphere (TOA). The observations at RRV suggest that the responsivities have changed by -9 ± 7 %, -1 ± 7 % and -4 ± 7 % for bands 1, 2, and 3, respectively, from the values corresponding to pre-launch calibration. In 2010 and 2011, the second and third campaigns were performed and the accuracy was improved by more frequent calibration of the surface albedo

AMTD
5, 2959–3018, 2012

measurements (Kuze et al., 2011d, 2012). As shown in Table 4a, the changes became slower 18 months after the launch. The Airborne Visible/InfraRed Imaging Spectrometer (AVIRIS) on ER-2 aircraft had flown over RRV twice at the time of GOSAT overpass on 9 October 2009 and 20 June 2011. Cross calibrations between AVIRIS and GOSAT independently corroborated the vicarious calibration results and shows the similar trend of the degradation. Further analysis is needed for AVIRIS data.

3.1.3 Solar calibration for SWIR

The back side of the Spectralon diffuser plate is exposed for a short time once a month. If the degradation is proportional to the exposure time, it is safe to assume that the back side has not been degraded. Therefore, the back side calibration data can monitor the relative degradation. The solar irradiance calibration measurements had been analyzed for three years. On 4 March 2009, by rotating the whole satellite itself, the incident angle dependence of the onboard Spectralon reflectivity was acquired. We used this data and applied linear interpolation for cosine effect correction instead of simply normalizing with cosine. For this analysis, the sun and earth seasonal variation in distance has been also corrected. Figure 8a shows the ratio between the front and back sides of the solar diffuser plate calibrations. The figure shows a large degradation in TANSO-FTS Band 1 on the diffuser's front surface, but slowing down of the degradation speed with time. Figure 8b shows monthly solar calibration data using the diffuser plate's back side. The curve indicates the on-orbit radiometric response change of the instrument itself. In the first year after the launch, the degradation of both the diffuser and the TANSO-FTS throughput was fast. However, the degradation became considerably slower in the following year. The vertical lines in the figures represent the time of the vicarious campaigns. The degradation between June 2009, 2010, and 2011 is summarized in Table 4b and c.

AMTD
5, 2959–3018, 2012

3.1.4 SWIR trend over the Sahara desert

The Sahara and Arabian deserts are virtually always clear all year round with almost no vegetation and water. We picked several sites as shown in Fig. 9a. The surface is not always Lambertian and the reflectance is dependent on solar the zenith angle. To estimate the degradation accurately, data from the same time of the year have to be compared. To minimize the random noise, several data in the same season are selected and averaged. Since August 2010, we used the 3-point cross-track scan mode as the nominal one. Earlier measurements were made primarily in 5-point cross-track scan mode. We compared June and July of 2009 and 2010 data using 5-point cross-track scan mode and 2011 data using 3-point cross-track scan mode. TANSO-FTS TIR data between 898 cm^{-1} and 929 cm^{-1} was used for cloud screening. If the maximum brightness temperature is lower than 292.5 K, we then assume that the data is contaminated by cloud. This screening process is applied only for the Sahara desert trend analysis. We recorded the spectral radiances of 12971.027 cm^{-1}, 6008.327 cm^{-1}, and 4806.9806 cm^{-1} in the analysis for bands 1, 2, and 3. Figure 9b shows the degradation of the TANSO-FTS throughput for the 5 sites in one year. The change in one year was derived from a weighted-average of the data over the sites, respectively, on the basis of the assumption that the aerosol optical thicknesses are the same. Since we cannot compare Sahara 8 and 9 sites shown in Fig. 9a from 3-point cross-track scan mode, we compared the data for June 2009, 2010 and 2011 at 3 sites instead. The results are summarized in Table 4b and c.

3.1.5 SWIR degradation estimation and correction

Even though X_{CO_2} and X_{CH_4} are retrieved by using differential absorption spectra, scattering by aerosol and the thin clouds in the real atmosphere is still not negligible. To distinguish the reflection from the surface and scattering from the atmosphere for accurate light path estimation, the throughput degradation has to be monitored in order to maintain the radiometric accuracy in the entire mission. Table 4 summarizes the degradation

AMTD
5, 2959–3018, 2012

derived from independent methods. From the vicarious calibration (absolute), onboard calibration using the solar diffuser plate (relative) and the data obtained for the analysis over the Sahara desert (relative), the analytical results are consistent. An agreement among the three independent methods for the estimation of one year degradation is within 3 % (peak to peak). All methods indicate the radiometric response degradation with time in both TANSO-FTS and CAI. Two types of degradation are observed. The first is the step change between the pre-launch value and the on-orbit initial value especially in TANSO-FTS Band 1 and CAI bands 1 and 4. The calibration on TANSO-CAI is to be discussed in the next section. The second type of degradation is the gradual on-orbit change. The largest degradation occurs at the shortest wavelengths. There are a few possible explanations for this step change: these explanations are as follows: (i) contamination during the launch or subsequent deployment, (ii) change in the modulation efficiency of the TANSO-FTS mechanism, which is sensitive to the thermal and mechanical environmental conditions and (iii) angular distribution correction error in the integrating sphere used for the pre-launch calibration. The gradual degradation may be attributed to contamination or changes in modulation efficiency. The upper part of Fig. 1 shows the schematics of the TANSO-FTS optics module. CAM is mounted between the pointing mirror and FTS-mechanism. CAM data over the Sahara has shown no significant degradation since the launch. The possible degradation occurs in modulation efficiency of the FTS mechanism or the aft-optics optical effciency.

Lunar calibration was performed twice a year since the launch, on 11 March and 9 April 2009, 28 April and 6 June 2010, and 18 April and 14 July 2011. The bidirectional reflectance distribution function (BRDF) for the lunar surface is not Lambertian and a complicated calibration is needed for absolute calibration. These data can be used for both TANSO-FTS and CAI absolute radiometric calibration. However, the lunar surface has a strong BRDF when the incident angle is zero. After the BRDF correction, the analytical results of the TANSO-CAI show a similar trend, but further investigations and BRDF corrections are needed. In case of TANSO-FTS, the size of the moon

AMTD
5, 2959–3018, 2012

disk viewed from the GOSAT orbit is about the half of the instantaneous field of view (IFOV): the analysis is more complicated.

On the basis of the vicarious absolute calibration, response correction factors have been derived as functions of time (days from the launch). By combining the pre-launch radiance conversion factor and these correction factors, the calibrated spectral radiance thus can be calculated. Because the surface reflectance over RRV and the solar diffuser reflectivity are high, the interferograms are calibrated with medium gain to avoid saturation. High gain response over the Australian desert can be compared by observing the same site with high and medium gains. The ratio between high and medium gains is determined by the feedback resistance of the amplifier. The comparison over the Australian desert indicated that the ratio is as designed. Thus, response correction factor derived from medium gain can be applied to the high gain data. Low gain has never been used since the launch.

3.1.6 Cross calibration and validation for TIR

TIR spectral radiance is calibrated frequently by looking at DS and the onboard BB. Onboard calibration accuracy does not change with time unless the temperature sensor is degraded. In parallel, cross calibration with other space borne instruments has been performed. The spectral radiance has been compared at high latitude by using simultaneous nadir overpasses of Infrared Atmospheric Sounding Interferometer (IASI). IASI data is found within 100 km of the GOSAT field of view and within 10° of nadir. The difference in brightness temperature between 200 K and 270 K is smaller than ±1 K (Knuteson, private communication, 28 February 2011). In addition, TIR vicarious calibration was performed at RRV in June 2011 by measuring surface temperature and emissivity by Atmospheric Emitted Radiance Interferometer (AERI) FTS together with upward spectral radiation by using the airborne Scanning High-resolution Interferometer Sounder (S-HIS) FTS (Tobin et al., 2006; Kuze et al., 2011d). For an atmospheric window region around 10 µm where the radiation from the surface is dominant, it is very difficult for IASI and GOSAT to view the exactly the same location at the same

AMTD
5, 2959–3018, 2012

time. The S-HIS data covered the entire IFOV of the TANSO-FTS and the target surface temperature of RRV is 320 K. However, we cannot compare the radiation from the atmosphere above the S-HIS flight altitude. Only satellite data can provide the thermal radiation spectra from the upper atmosphere where the radiation from the surface is fully absorbed. A combination of formation flight of a high- altitude (20 km) aircraft and match-up data from other satellites can calibrate the wide range of spectral radiance from both atmosphere and ground surface. Both cross calibrations with IASI and S-HIS agree well within ±1 K. We still are continuously comparing and analyzing these data.

3.2 Signal-to-noise ratio

There is no stable onboard white light source available today for radiometric calibration purposes. Therefore, SNR cannot be measured explicitly. It is estimated from the imaginary spectra or out-of-the band real spectra. The noise level is the same as the one we measured before the launch, and there is no significant response degradation. Thus, we can expect the SNR performance to be reasonably similar to the one described by Kuze et al. (2009). There are two dominant noise sources for TANSO-FTS bands 1, 2, and 3. One is the detector and its electronics noise, which is independent of the input signal level and proportional to the square root of the band width. The performance can be measured with dark input data and can be expressed with specific detectivity (D^*). The second source is the shot noise, which is proportional to the square root of the total number of input photons. Band 2 has wide band width of 5800–6400 cm^{-1} to cover CO_2, CH_4 and H_2O lines, while the shot noise contribution is larger than in the other two bands.

AMTD
5, 2959–3018, 2012

3.3 Spectral resolution and instrument line shape function

3.3.1 Pre-launch calibration and simulated model

The geophysical parameters are retrieved by comparing the measured spectral radiance and the simulated radiance at the top of the atmosphere. X_{CO_2}, X_{CH_4}, and other geophysical parameters such as surface pressure can be retrieved by minimizing the residual between the measured spectrum and simulated spectrum convoluted with the instrument line shape function (ILSF). Because ILSF is a function of the wavelength, ILSFs at selected wavelengths are modeled as shown in Fig. 10a. The models are simulated because the pre-launch tests with monochromatic light source were performed at limited wavenumbers and did not cover the whole spectral range. Off-axis mounting of the detector due to imperfect alignment creates an asymmetry of ILSF: however, this effect can be numerically simulated. ILSF of short wavelengths is more sensitive to the misalignment, thus the detector position during the integration has to be accurately measured. Misalignment from the ideal optical axis of the Band 1P and 1S are estimated by introducing monochromatic light prior to the launch. Both spatial and angular uniformity of the input light over the scene aperture and IFOV are particularly important for this characterization. Although the pre-launch test configuration was imperfect, nevertheless the data contains detector offset information. By carefully simulating the imperfect pre-launch test configuration, the offset value was estimated. The best estimate ILS models were calculated using the offset value and optical aberration. On the other hand, for bands 2, 3, and 4, ILSF are insensitive to the misalignment of the detector, which is less than 50 µm, and only the finite size effect of IFOV have been considered.

3.3.2 Spectral resolution on orbit

Figure 10b shows the long term stability of the data using onboard ILSF calibration laser input. Although the diode laser is not temperature controlled and the wavelength

AMTD
5, 2959–3018, 2012

is not constant, the ILSF shape itself is very stable: this indicates that no significant spectral resolution change has been observed.

3.3.3 Absolute spectral calibration

By carefully monitoring sampling laser output level of the FTS mechanism and the solar Fraunhofer line position, we have observed a gradual decrease of the laser signal detection level and an increase of the apparent wavenumber of the Fraunhofer lines. The degradation is exponential and smaller than 10 % in one year and the degradation is becoming slower. We expect the laser has sufficient level of control after 10 yr of operation. Because all the bands of 1, 2 and 3 have the constant wavenumber shift, the most probable cause is the optical alignment change of the laser beam on orbit as illustrated in Fig. 11. Consequently, MOPD has become larger and spectral resolution has become slightly higher. The absolute spectral position can be calibrated by applying the spectral correction factor with time:

$$\nu_{\mathrm{corre}} = \nu_{\mathrm{raw}} / (a_0 \exp(a_1 t) + a_2), \tag{8}$$

where ν_{corre}, ν_{raw} are wavenumber before and after the correction, and a_0 ,a_1 ,a_2, and t are the calibration coefficients and time from the launch. As shown in Fig. 12, the change since the launch is less than 10 ppm and the effect on spectral resolution is negligibly small.

3.4 Geolocation and pointing characterization

The optical mirror pointing mechanism has two different speed motions; IMC and pointing of the earth surface during turnarounds. This complicated control is sensitive to electromagnetic and micro-vibration environments. The angular resolvers of the two axis motors are the only devices to provide geometrical information for the onboard control as well as the data analysis on the ground. The resolvers are sensitive to electromagnetic environment and suspect to have errors, which are of two kinds. One kind

AMTD
5, 2959–3018, 2012

of error is a known offset (predictable) that the onboard resolver can detect and that the Level 1B process can correct. The other is an unpredictable error, which the resolver can not detect. The error is a possible resolver anomaly most likely due to the noise affected by the electromagnetic interference. The second error was first detected just three months after the launch (April 2009) and had not been stable until August 2009. To estimate the offset values, we use image acquired with the Advanced Visible and Near Infrared Radiometer type 2 (AVNIR-2) on the Advanced Land Observing Satellite (ALOS) (Tadono et al., 2009) and CAM data of the ground correction points (GCP). There is no general formula to express the pointing error. Instead we have been providing the offset information since September 2009 and the example is shown in Table 5. Offset values have slowly changed with time. It is a function of the scanning pattern and not of other considerations, such as the location on Earth. Regarding the pointing error, settling down (overshoot) is not ideal when the AT range of motion is large. The offset level is not a simple linear function of AT and CT angle. Hence, the geometrical correction in the 3-point cross-track scan mode is not the same as that in the target mode and 5-point cross-track scan mode.

3.5 Polarimetric calibration by Mueller matrix

Both instrument and scene flux scattered by the earth's atmosphere have large polarization. The protection coating on the pointing mirror made of silver surface has a polarization phase. To calculate the response to the polarized input scene flux, the polarization reflectivity and phase of the instrument need to be considered. The relation between input flux Stokes vector and two linear polarizations "P" and "S" of TANSO-FTS measurements can be expressed using the Mueller matrix as follows:

$$\boldsymbol{S}_{\text{Poutput}} = \mathbf{M}_{\text{pp}}\mathbf{M}_{\text{opt}}\mathbf{M}_{\text{r}}(-\theta_{\text{CT}})\mathbf{M}_{\text{p}}(\theta_{\text{AT}})\mathbf{M}_{\text{m}}(\theta_{\text{AT}})\mathbf{M}_{\text{r}}(\theta_{\text{CT}})\boldsymbol{S}_{\text{input}}, \quad (9)$$

$$\boldsymbol{S}_{\text{Soutput}} = \mathbf{M}_{\text{ps}}\mathbf{M}_{\text{opt}}\mathbf{M}_{\text{r}}(-\theta_{\text{CT}})\mathbf{M}_{\text{p}}(\theta_{\text{AT}})\mathbf{M}_{\text{m}}(\theta_{\text{AT}})\mathbf{M}_{\text{r}}(\theta_{\text{CT}})\boldsymbol{S}_{\text{input}}, \quad (10)$$

where $\mathbf{M}_{\text{pp}}$, $\mathbf{M}_{\text{ps}}$, $\mathbf{M}_{\text{opt}}$, $\mathbf{M}_{\text{p}}$, $\mathbf{M}_{\text{m}}$, and $\mathbf{M}_{\text{r}}$ are Muller matrixes of polarization beam splitter, optical efficiency of the FTS-mechanism and aft-optics, phase difference due to the

AMTD
5, 2959–3018, 2012

pointing mirror surface coating, pointing mirror reflectivity, and CT rotation, respectively. $\boldsymbol{S}_{\text{Poutput}}$, $\boldsymbol{S}_{\text{Soutput}}$, $\boldsymbol{S}_{\text{input}}$, θ_{CT}, and θ_{AT} are output and input signals of the Stokes vector and the CT and AT angles, respectively. $\boldsymbol{S}_{\text{input}}$ is the Stokes vector at the top of the atmosphere can be calculated with a vector radiative transfer model. By comparing simulated I component of the Stokes vector $\boldsymbol{S}_{\text{Poutput}}$ and $\boldsymbol{S}_{\text{Soutput}}$($I_{\text{PopC}}$ and I_{SopC}) and I_{PopM} and I_{SopM} measured spectral radiance measured with TANSO-FTS, X_{CO_2} and X_{CH_4} can be independently retrieved from SWIR P and S bands. The reference plane for polarization for the input Stokes vector (I, Q, U, and V) is defined by the local normal at the target and the ray from the target to the satellite. The pre-launch radiometric calibration was performed on the ground by introducing un-polarized light from nadir, of which input and output spectral radiance are I_{ipPL}, I_{PopPL} and I_{SopPL}, respectively. The prelaunch calibration data with the Level 1 format can be expressed in $R_{\text{P}}\left(I_{\text{PopPL}}\right)$ and $R_{\text{S}}\left(I_{\text{SopPL}}\right)$. The radiance conversion table prepared prelaunch shows the relation between I_{ipPL}, $R_{\text{P}}\left(I_{\text{PopPL}}\right)$, and $R_{\text{S}}\left(I_{\text{SopPL}}\right)$ as shown in Fig. 7. I_{PopPL} and I_{SopPL} are not used explicitly in radiometric calibration.

The above mentioned Mueller matrix needs to be used to correct the AT and CT angles dependency of the pointing mirror in the case of slant looking. Thus the correction requires the pointing mirror reflectivity and phase information in $\mathbf{M}_{\text{p}}$ and $\mathbf{M}_{\text{m}}$ as the function of AT angle (the incident angle to the mirror) as indicated in Figs. 13 and 14a. These data are acquired with the mirror witness sample, which was coated at the same time as the flight mirrors. Aft-optics is calibrated pre-launch as the overall response including the pointing mirror, fold mirror, FTS mechanism, and telescope and the individual optical efficiency is not needed for the radiometric calibration for the on-orbit data. This coating has been optimized for SWIR region with higher than 99 % reflectivity and the AT angle dependency of SWIR bands is very small.

However, the reflectivity is lower and the polarization sensitivity is higher in some TIR wavelength, as shown in Fig. 14b. As discussed in Sect. 2.5, measured spectral radiance $\boldsymbol{S}_{\text{Toutput}}$ can be expressed using the scene flux $\boldsymbol{S}_{\text{Tinput}}$, thermal radiation from

AMTD
5, 2959–3018, 2012

the pointing mirror, and the back ground radiation in the following Mueller matrix:

$$\boldsymbol{S}_{\text{Toutput}} = \mathbf{M}_{\text{opt}}\mathbf{M}_{\text{r}}(-\theta_{\text{CT}})\mathbf{M}_{\text{m}}(\theta_{\text{AT}})\mathbf{M}_{\text{r}}(\theta_{\text{CT}})\boldsymbol{S}_{\text{Tinput}} + \mathbf{M}_{\text{opt}}\mathbf{M}_{\varepsilon}(-\theta_{\text{CT}})\boldsymbol{S}_{\text{Tmirror}} + \Delta\boldsymbol{S}_{\text{BG}}, \quad (11)$$

where $\boldsymbol{S}_{\text{Tmirror}}$ and $\Delta\boldsymbol{S}_{\text{BG}}$ are Stokes vector of the radiation from the pointing mirror, and the back ground radiation variation between calibrations, respectively. *I* component of $\boldsymbol{S}_{\text{Tinput}}$ is retrieved from Eq. (11) in the TIR Level 1 processing.

3.6 Quality flag of data products

All the data transmitted to the ground are processed to the Levels 1A and 1B products, contained with some low quality data. In the Level 1 processing, quality is checked and data with problems can be clearly identified with flags, as listed in Table 6. The quality flag of spike noise flag in the Level 1B product shows both fluctuation of the interferogram and spike caused by the cosmic rays. For the last three years after the launch, no spike caused by the cosmic ray has been detected. The FTS mechanism scan speed instabilities larger than 2 % are to be detected by monitoring the passing time of the 10 different OPD positions. However, the stability on orbit is much better than 1 % and the speed instability has never been detected since the launch.

3.7 Additional corrections

Methods of conversion, calibration and corrections are described in this paper. The Level 1 products and calibration data include all the information required to produce the Level 2 products. In parallel, for the detailed Level 1 product analysis, the additional software is prepared to correct the data additionally:

(i) Finite size of the field of view; finite size of the field of view has a self-apodization effect. Without large degradation of the spectral shape, the self-apodization due to the size is corrected as described by Knuteson et al. (2004).

AMTD
5, 2959–3018, 2012

(ii) Wavelength shift correction; the shift due to the optical alignment change of the sampling laser is corrected even though the value of the shift since the launch is small enough.

(iii) Mueller matrix; four-by-four elements for 3 TANSO-FTS SWIR bands are added to the Level 1 data.

(iv) Geometric correction; the most probable offset correction of the optical mirror pointing mechanism estimated from CAM data is applied.

(v) Spectral radiance conversion: the Level 1 data of which unit is V cm is converted to the calibrated spectral radiance of which unit is $W\,cm^{-2}\,str^{-1}\,cm$.

4 TANSO-CAI Level 1A data processing, characterization, and calibration

The design and pre-launch performance and calibration of TANSO-CAI were described in detail in Kuze et al. (2009). The TANSO-CAI Level 1A data processing, on-orbit performance and calibration are described in this section. Instruments models and calibrations are summarized in Tables 2. and 3. JAXA has been providing the raw Level 1 data to NIES and other users. In this section, we describe how to correct the raw data and convert it to the spectral radiance.

4.1 Radiometric calibration and correction

All the pixels of 4 TANSO-CAI bands were calibrated using the integrating sphere (Kuze et al., 2009; Sakuma et al., 2010). Radiometric calibration is based on the pre-launch calibration and the data are corrected with the following processes.

AMTD
5, 2959–3018, 2012

4.1.1 Offset extraction and spectral radiance conversion

The TANSO-CAI Level 1A data includes signals, offsets which vary depending on the total input radiance, and dark currents. The observed spectral radiance is calculated by extracting the offset and dark current using the following equation:

$$S_{\mathrm{obs}}(n) = \frac{V_{\mathrm{C}}(n) - V_{\mathrm{Cpre}} - V_{\mathrm{Cdark}}(n, T_{\mathrm{int}})}{T_{\mathrm{int}} R_{\mathrm{C}}(n)}, \tag{12}$$

where $V_{\mathrm{C}}(n)$, $V_{\mathrm{Cdark}}(n)$, and $R_{\mathrm{C}}(n)$ are output, dark level, and response of the pixel number n, respectively. T_{int} is the integration time of the detectors. V_{Cpre} is the average of output of the first three pre-scan pixels and calculated separately for the odd and the even pixels. We assume that the dark level is the function of the integration time and is constant with time since the launch. $R_{\mathrm{C}}(n)$ is based on the pre-launch calibration and degradation correction is described below.

4.1.2 Pixel-to-pixel non-uniformity correction

All the pixels of each band were calibrated at the same time before the launch by using the integrating sphere, the inner surface of which is coated with barium sulfate ($BaSO_4$). Radiation from the aperture of the integrating sphere has angular distribution especially for bands 1 (UV) and 4 (SWIR). Spectral radiance of the integrating sphere was calibrated at a direction perpendicular to the aperture and its angular distribution was not calibrated before the launch. As TANSO-CAI has a wide field of view, the pre-launch data other than the center pixel has to be corrected as follows. The telescope optics of bands 1 and 4 have very small limb darkening while bands 2 and 3 have large limb darkening. Therefore, the angular distribution of bands 1 and 4 can be corrected. To check pixel-to-pixel uniformity, we assume the earth albedo is uniformly distributed when TANSO-CAI data acquired from all the 44 paths averaged over one year. The earth albedo is defined as the measured reflectance at the top of the atmosphere. By correcting Rayleigh scattering and sun glint effect, pixel-to-pixel non-uniformity can be

AMTD
5, 2959–3018, 2012

detected and corrected using the averaged measured data for Band 1. There was no need for pixel-to-pixel correction for Band 2. For Band 3, local bump structures are corrected using one-year averaged data. Band 4 is corrected using one-year averaged data, except for several pixels, of which dark current have increased. Pixel 154 shows the sudden increase after passing through the South Atlantic Anomaly. The data shown in Fig. 15 is the pixel-to-pixel non-uniformity correction of Band 1. These corrected radiance conversion factors are used for the TANSO-CAI Level 1B+ and Level 2 product.

4.1.3 Degradation after the launch

The vicarious calibrations at RRV indicate that the difference between pre-launch and initial on-orbit response is large in TANSO-CAI bands 1 and 4 but that the response change with time on orbit seems to be slow for all bands. Another method to check the degradation is a formation airplane flight with GOSAT (Kuze et al., 2012). The preliminary comparison between AVIRIS and TANSO-CAI lead to similar calibration results compared to the vicarious calibration. The last method is the comparison of the data over the Sahara desert as we did for TANSO-FTS. We had used the TANSO-CAI data between June of 2009, 2010 and 2011. First, we selected the site data where standard deviation of the measured earth albedo between 3 by 3 pixels of TANSO-CAI was lower than 0.005. Second, we used the sites where normalized difference vegetation index (NDVI) is smaller than 0.01. The one year degradation of each site is presented in Fig. 16. The variation of the measured earth albedo differs from site to site and the weighted averages of response change over the 17 sites in one year of TANSO-CAI bands 1, 2, 3, and 4 are summarized in Table 4b and c. Lunar calibrations also have been performed six times since the launch. In addition to the difficulty to correct BRDF of lunar surface, the non-uniformity of the lunar surface reflectance has to be considered for TASNO-CAI. At present, lunar calibration data have not been used for radiometric degradation estimation. As illustrated in the lower part of Fig. 1, the TANSO-CAI optics have simpler configuration than FTS and now the response becomes stable for all bands.

AMTD
5, 2959–3018, 2012

4.2 Geolocation

The exact viewing vector of the each pixel was geometrically calibrated before the launch with the collimator in the laboratory. As the optical aberration and misalignment of the off-axis pixels become larger, the geometrical model of both AT and CT directions can be well expressed using the 3rd order of polynomials as described below. After the launch, coefficients have been revised using ground calibration points (GCP). But, the difference from the pre-launch values is very small.

$$\theta_{\mathrm{atc}} = p_{\mathrm{x0m}} + p_{x1}(n - n_{\mathrm{c}}) + p_{x2}(n - n_{\mathrm{c}})^2 + p_{x3}(n - n_{\mathrm{c}})^3, \quad (13)$$

$$\theta_{\mathrm{ctc}} = p_{y0} + p_{y1}(n - n_{\mathrm{c}}) + p_{y2}(n - n_{\mathrm{cm}})^2 + p_{y3}(n - n_{\mathrm{c}})^3. \quad (14)$$

In the above equations, p are coefficients of the polynomials, θ_{atc} and θ_{atc} are the AT and CT angles from the nadir, n is the pixel number and n_{c} is the center pixel number. In the TANSO-CAI Level 1B, 1B+, and 2 data, the geolocation is corrected using the above equations and digital elevation model (DEM) data. Only Band 4 uses a 512-pixels InGaAs-detector and complementary metal oxide semiconductor (CMOS) readouts. Odd and even number pixels have two slightly different directions of read-outs respectively. The detector readout masks for even number pixels are not opaque enough and its field of view has been stretched. These anomalies are minimized by shifting the geolocation separately for the odd and the even pixels in the TANSO-CAI Level 1B, 1B+, and Level 2 products.

5 Conclusions

Almost three years have passed since the launch, and the overall functions and performances are successful and they are well within design objectives. TANSO-FTS is

AMTD
5, 2959–3018, 2012

operating regularly with almost 100 % duty and the Level 1 is processed and distributed to NIES, NASA, and ESA typically within 5 h after observation. No significant degradation of SNR and spectral resolution has been observed. A few anomalies were found onboard, but they have stabilized since. The Level 1 algorithms have been updated since the launch in order to correct these anomalies. The algorithms include the quality information for the higher level processing to investigate the data quality. Together with the Level 1B data and pre-launch calibration data, degradation correction factors have been determined. GOSAT continues its observations and has been providing well-calibrated high spectral resolution data.

Acknowledgements. The authors would like to thank the GOSAT science team and the operation team. We especially acknowledge Henry Buijs and Raphael Desbiens of ABB BOMEM Inc.; Hank Revercomb and Robert Knuteson of University of Wisconsin; Annmarie Eldering, David Crisp, Charles Miller, Christian Frankenberg, Denis O'Brien, Tommy Taylor, and Paul Wennberg of NASA-ACOS team; Tatsuya Yokota, Hiroshi Watanabe, Nobuyuki Kikuchi, and Yukio Yoshida of NIES; Andre Butz of Karlsruhe Institute of Technology; Atsushi Takeuchi of NEC Toshiba Space Systems Inc.; and Mayumi Yoshida, Riko Higuchi, Nami Sekio, and Yasushi Mitomi of Remote Sensing Technology Center.

References

Butz, A., Guerlet, S., Hasekamp, O., Schepers, D., Galli, A., Aben, I., Frankenberg, C., Hartmann, J.-M., Tran, H., Kuze, A., Keppel-Aleks, G., Toon, G., Wunch, D., Wennberg, P., Deutscher, N., Griffith, D., Macatangay, R., Messerschmidt, J., Notholt, J., and Warneke, T.: Toward accurate CO_2 and CH_4 observations from GOSAT, Geophys. Res. Lett., 38, L14812, doi:10.1029/2011GL047888, 2011.

Crisp, D., Fisher, B. M., O'Dell, C., Frankenberg, C., Basilio, R., Bösch, H., Brown, L. R., Castano, R., Connor, B., Deutscher, N. M., Eldering, A., Griffith, D., Gunson, M., Kuze, A., Mandrake, L., McDuffie, J., Messerschmidt, J., Miller, C. E., Morino, I., Natraj, V., Notholt, J., O'Brien, D. M., Oyafuso, F., Polonsky, I., Robinson, J., Salawitch, R., Sherlock, V., Smyth, M., Suto, H., Taylor, T. E., Thompson, D. R., Wennberg, P. O., Wunch, D., and Yung, Y. L.:

AMTD
5, 2959–3018, 2012

The ACOS CO_2 retrieval algorithm – Part II: Global X_{CO_2} data characterization, Atmos. Meas. Tech., 5, 687–707, doi:10.5194/amt-5-687-2012, 2012.
Frankenberg, C., Butz, A., and Toon, G. C.: Disentangling chlorophyll fluorescence from atmospheric scattering effects in O_2 A-band spectra of reflected sun-light, Geophys. Res. Lett., 38, L03801, doi:10.1029/2010GL045896, 2011a.
Frankenberg, C., Fisher, J. B., Worden, J., Badgley, G., Saatchi, S. S., Lee, J.-E., Toon, G. C., Butz, A., Jung, M., Kuze, A., and Yokota, T.: New global observations of the terrestrial carbon cycle from GOSAT: Patterns of plant fluorescence with gross primary productivity, Geophys. Res. Lett., 38, L17706, doi:10.1029/2011GL048738, 2011b.
Guanter, L., Frankenberg, C., Dudhia, A., Lewis, P. E., Gomez-Dans, J., Kuze, A., Suto, H., and Grainger, R. G.: Retrieval and global assessment of terrestrial chlorophyll fluorescence from GOSAT space measurements, Remote Sens. Environ., 121, 236–251, 2012.
Ishida, H., Nakajima, T. Y., and Nakajima, T.: Development of an unbiased cloud detection algorithm for a spaceborne multispectral imager, J. Geophys. Res., 114, D07206, doi:10.1029/2008JD010710, 2009.
Ishida, H., Nakajima, T. Y., Yokota, T., Kikuchi, N., and Watanabe, H.: Investigation of GOSAT TANSO-CAI cloud screening ability through an intersatellite comparison, J. Appl. Meteor. Climatol., 50, 1571–1586, 2011.
Joiner, J., Yoshida, Y., Vasilkov, A. P., Yoshida, Y., Corp, L. A., and Middleton, E. M.: First observations of global and seasonal terrestrial chlorophyll fluorescence from space, Biogeosciences, 8, 637–651, doi:10.5194/bg-8-637-2011, 2011.
Joiner, J., Yoshida, Y., Vasilkov, A. P., Middleton, E. M., Campbell, P. K. E., Yoshida, Y., Kuze, A., and Corp, L. A.: Filling-in of far-red and near-Infrared solar lines by terrestrial and atmospheric effects: simulations and space-based observations from SCIAMACHY and GOSAT, Atmos. Meas. Tech. Discuss., 5, 163–210, doi:10.5194/amtd-5-163-2012, 2012.
Keppel-Aleks, G., Toon, G. C., Wennberg, P. O., and Deutscher, N. M.: Reducing the impact of source brightness fluctuations on spectra obtained by Fourier-transform spectrometry, Appl. Opt., 46, 4774–4779, 2007.
Knuteson, R. O., Revercomb, H. E., Best, F. A., Ciganovich, N. C., Dedecker, R. G. Dirkx, T. P., Ellington, S. C., Feltz, W. F., Garcia, R. K., Howell, H. B., Smith, W. L., Short, J. F., and Tobin, D. C.: Atmospheric Emitted Radiance Interferometer. Part II: Instrument Performance, J. Atmos. Ocean Tech., 21, 1777–1789, 2004.

AMTD
5, 2959–3018, 2012

Kuze, A., Suto, H., Nakajima, M., and Hamazaki, T.: Thermal and near infrared sensor for carbon observation Fourier-transform spectrometer on the Greenhouse Gases Observing Satellite for greenhouse gases monitoring, Appl. Opt., 48, 6716–6733, 2009.

Kuze, A., O'Brien, D. M., Taylor, T. E., Day, J. O., O'Dell, C., Kataoka, F., Yoshida, M., Mitomi, Y., Bruegge, C., Pollock, H., Basilio, R., Helmlinger, M., Matsunaga, T., Kawakami, S., Shiomi, K., Urabe, T., and Suto, H.: Vicarious calibration of the GOSAT sensors using the Railroad Valley desert playa, IEEE T. Geosci. Remote Sens., 49, 1781–1795, doi:10.1109/TGRS.2010.2089527, 2011a.

Kuze, A., Suto, H., Shiomi, K., and Nakajima, M.: GOSAT TANSO Calibration and characterization of 2 Years on orbit operation, ISTS, Proceedings of The 28th International Symposium on Space Technology and Science (ISTS), Okinawa, 2011b.

Kuze, A., Suto, H., Shiomi, K., and Nakajima, M.: Lessons learned from GOSAT and improvements for the next mission, Hyperspectral Imaging and Sounding of the Environment, OSA Technical Digest (CD) (Optical Society of America, 2011), paper JMA3, 2011c.

Kuze, A., Bruegge, C., O'Brien, D. M., Knuteson, R. O., and Yates, E.: Vicarious calibration and validation campaign of the GOSAT sensors at Railroad Valley, AGU fall meeting Suppl., Abstract A42D–07, 2011d.

Kuze, A., Kataoka, F., O'Brien, D. M., Taylor, T. E., Mitomi, Y., Bruegge, C., Crisp, D., Pollock, H., Helmlinger, M., Schwandner, F., Urabe, T., Kawakami, S., Shiomi, K., Ohyama, H., Suto, H., Tanaka, T., Naito, M., Harada, M., and Inoue, M.: GOSAT sensors on orbit radiometric characterization by vicarious and onboard calibrations, to be submitted, 2012.

O'Dell, C. W., Connor, B., Bösch, H., O'Brien, D., Frankenberg, C., Castano, R., Christi, M., Eldering, D., Fisher, B., Gunson, M., McDuffie, J., Miller, C. E., Natraj, V., Oyafuso, F., Polonsky, I., Smyth, M., Taylor, T., Toon, G. C., Wennberg, P. O., and Wunch, D.: The ACOS CO_2 retrieval algorithm – Part 1: Description and validation against synthetic observations, Atmos. Meas. Tech., 5, 99–121, doi:10.5194/amt-5-99-2012, 2012.

Parker, R., Boesch, H., Cogan, A., Fraser, A., Feng, L., Palmer, P. I., Messerschmidt, J., Deutscher, N., Griffith, D. W.T., Notholt, J., Wennberg, P. O., and Wunch, D.: Methane observations from the Greenhouse Gases Observing SATellite: Comparison to ground-based TCCON data and model calculations, Geophys. Res. Lett., 38, L15807, doi:10.1029/2011GL047871, 2011.

Saitoh, N., Imasu, R., Ota, Y., and Niwa, Y.: CO_2 retrieval algorithm for the thermal infrared spectra of the Greenhouse Gases Observing Satellite: potential of retrieving

AMTD
5, 2959–3018, 2012

CO_2 vertical profile from high-resolution FTS sensor, J. Geophys. Res. 114, D17305, doi:10.1029/2008JD011500, 2009.
Sakuma, F., Bruegge, C., Rider, D., Brown, D., Geier, S., Kawakami, S., and Kuze, A.: OCO-GOSAT preflight cross calibration experiment, IEEE T. Geosci. Remote Sens., 48, 585–599, 2010.
Simon, A. R.: Data processing pipelines tailored for imaging Fourier-transform spectrometers, University of Laval, 2008.
Suto, H. and Kuze, A., : Correction of scan-speed instability of TANSO-FTS on GOSAT, AGU fall meeting Suppl., Abstract A51C-0107, 2010.
Suto, H., Kuze, A., Shiomi, K., and Nakajima, M.,: Updated Level-1 processing after two-years operation of TANSO-FTS, Proc. SPIE, 8154, 81541A, doi:10.1117/12.893405, 2011a.
Suto, H., Frankenberg, C., Crisp, D., and Kuze, A.: Characterization and correction of non-linearity effect on oxygen spectra of TANSO-FTS onboard GOSAT, AGU fall meeting Suppl., Abstract A33C-0210, 2011b.
Tadono, T., Shimada, M. Murakami, H., and Takaku, J.: Calibration of PRISM and AVNIR-2 Onboard ALOS "Daichi", IEEE T. Geosci. Remote Sens., 47, 4042–4050, 2009.
Tobin, D. C., Revercomb, H. E., Knuteson, R. O., Best, F. A., Smith, W. L., Ciganovich, N. N., Dedecker, R. G., Dutcher, S., Ellington, S. D., Raymond K., Garcia, H., Howell, B., LaPorte, D. D., Mango, S. A., Pagano, T. S., Taylor, J. K., Delst, P., Vinson, K. H., and Werner, M. W.: Radiometric and spectral validation of Atmospheric Infrared Sounder observations with the aircraft-based Scanning High-Resolution Interferometer Sounder, J. Geophys. Res. 111, D09S02, doi:10.1029/2005JD006094, 2006.
Yoshida, Y., Ota, Y., Eguchi, N., Kikuchi, N., Nobuta, K., Tran, H., Morino, I., and Yokota, T.: Retrieval algorithm for CO_2 and CH_4 column abundances from short-wavelength infrared spectral observations by the Greenhouse gases observing satellite, Atmos. Meas. Tech., 4, 717–734, doi:10.5194/amt-4-717-2011, 2011.

AMTD
5, 2959–3018, 2012

Table 1. TANSO-FTS data product format. Data level, data product, data format, and responsible institution.

Data level	Data product	Data format	Responsible institution
1A	Raw interferograms	HDF	JAXA
1B	Spectral radiance	HDF	JAXA
2	X_{CO_2} and X_{CH_4} soundings	HDF	NIES
3	Global distribution of X_{CO_2} and X_{CH_4}	HDF	NIES
4	CO_2 sources/sinks	NetCDF	NIES

AMTD
5, 2959–3018, 2012

Table 2. TANSO-FTS and CAI models.

		Number of models	Notes (conversion and relations)
Radiometric	FTS	3 bands by 2 linear polarizations and by 2 gains	Level 1B Spectra in V cm > Spectral radiance
Spectroscopic	CAI	4 bands, dark current model	Level 1 A data and integration time > Spectral radiance
	FTS	4 bands (16 ILSFs)	ILSF for convolution
Geometric	CAI	4 bands	Spectral response
	FTS	–	Pointing mirror angle > Viewing vector
Polarization	CAI	4 bands (AT and CT)	Pixel number > Viewing vector
	FTS	3 bands (Mueller matrix)	P, S output and 2 Stokes parameters

AMTD
5, 2959–3018, 2012

Table 3. TANSO-FTS and CAI correction factors.

		Number of models	Functions
Radiometric	FTS	3 bands by 2 Linear polarizations	Days from the launch
	CAI	4 bands	Days from the launch
Spectroscopic	FTS	Common value for all 4 bands	Days from the launch
Geometric	FTS	–	Combination of AT and CT angels

AMTD
5, 2959–3018, 2012

Table 4. Estimated degradations of radiometric responsivity for TANSO-FTS and CAI from four independent methods: (a) difference from pre-launch value and initial on-orbit calibration: degradation in one year (relative): (b) between June 2009 and June 2010 and (c) between June 2010 and June 2011.

(a)

		TANSO-FTS			TANSO-CAI			
		B1	B2	B3	B1	B2	B3	B4
Vicarious calibration	June 2009	−11 %	−1 %	−3 %	−17 %	+4 %	0 %	−18 %
	June 2010	−14 %	−2 %	−5 %	−20 %	−3 %	−4 %	−19 %
	June 2011	−14 %	−4 %	−6 %	−22 %	−7 %	−6 %	−20 %

(b)

Between June 2009 and June 2010	TANSO-FTS			TANSO-CAI			
	B1	B2	B3	B1	B2	B3	B4
Vicarious calibration	−3 %	−1 %	−2 %	−3 %	−7 %	−4 %	−1 %
Solar diffuser plate	−2.4 %	−0.7 %	0.0 %	N/A	N/A	N/A	N/A
Sahara Desert	−2.0 %	+0.2 %	−0.2 %	−1.7 %	−3.9 %	−0.7 %	−0.3 %
Average of bands P and S.							

(c)

Between June 2010 and June 2011	TANSO-FTS			TANSO-CAI			
	B1	B2	B3	B1	B2	B3	B4
Vicarious calibration	0 %	−2 %	−1 %	−2 %	−4 %	−2 %	−1 %
Solar diffuser plate	−0.6 %	−0.2 %	+0.1 %	N/A	N/A	N/A	N/A
Sahara desert	−0.9 %	−0.5 %	−0.2 %	+0.2 %	−1.3 %	−0.4 %	−0.6 %

Average of bands P and S.

AMTD
5, 2959–3018, 2012

Table 5. TANSO-FTS pointing onboard anomaly and correction: upper table is for the 5-point cross-track mode scan and lower one is for the 3-point cross-track scan mode. IDs in the tables are illustrated in Fig. 2. These are typical values and the offsets have changed with time.

(a) 5-point cross-track scan mode.

ID	AT (km)	Direction	CT (km)	Direction
0	8.3	positive down track*	2.1	the left of the ground track**
1	−0.5	negative down track	−0.4	
2	0.0	positive down track	−0.6	
3	−0.7	negative down track	−0.6	the right of the ground track
4	−0.1		−0.4	
5	9.2	positive down track	2.0	the left of the ground track
6	0.7		−0.1	the right of the ground track*
7	−0.3		−0.3	
8	−1.1	negative down track	−0.4	the right of the ground track
9	−1.3		−0.5	

(b) 3-point cross-track scan mode (typical values)

ID	AT (km)	Direction	CT (km)	Direction
0	5.0		3.0	
1	5.1		3.0	
2	5.4		3.2	
3	5.2		2.6	
4	5.2		2.8	
5	5.2		2.8	
6	5.7		3.5	
7	6.1		3.7	
8	5.8		3.6	
9	6.0		3.0	
10	5.9	positive down track	3.0	the left of the ground track
11	5.8		3.0	
12	6.2		2.9	
13	6.2		3.0	
14	6.2		3.0	
15	5.0		3.5	
16	5.0		3.6	
17	5.6		3.7	

*forward looking = looking south-south-west at the equator for the descending track (dayside).
** left of the ground track = the east-south-east at the equator for the descending track (dayside).

AMTD
5, 2959–3018, 2012

Table 6. TANSO-FTS quality flags.

Source	Item	Criteria
Satellite	Orbit control	Data acquired during orbit control
FTS	Saturation	Interferogram salutation, Blackbody temperature
	Spike	Fluctuation, Cosmic ray
	Low frequency disturbance (jitter)	Satellite and point mechanism micro vibration
	Pointing error	AT and CT pointing error larger than 0.1deg
	FTS mechanism temperature	Lower than 20° or higher than 26°
	Large ZPD position shift	Shift larger than 100 laser fringes
	Scan speed instability	FTS scan speed instability larger than 2 %

AMTD
5, 2959–3018, 2012

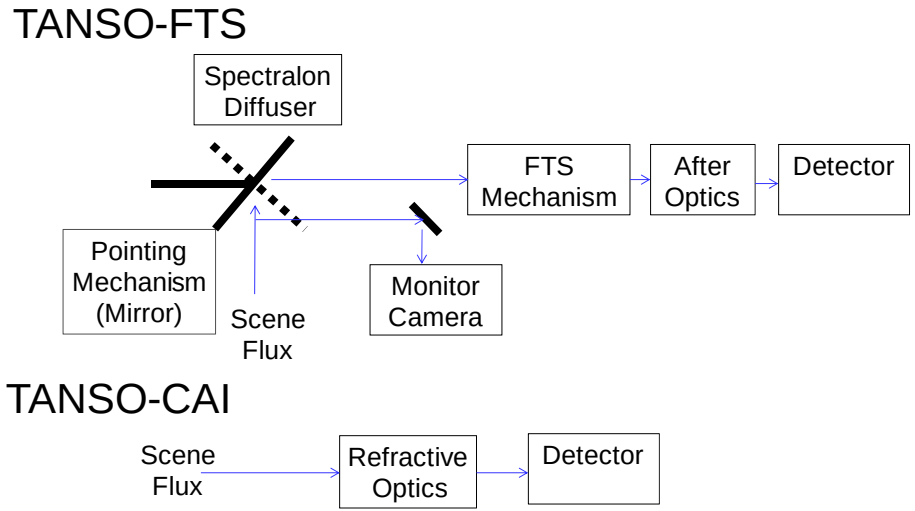

Fig. 1. The schematics of the TANSO-FTS and CAI optics modules.

AMTD
5, 2959–3018, 2012

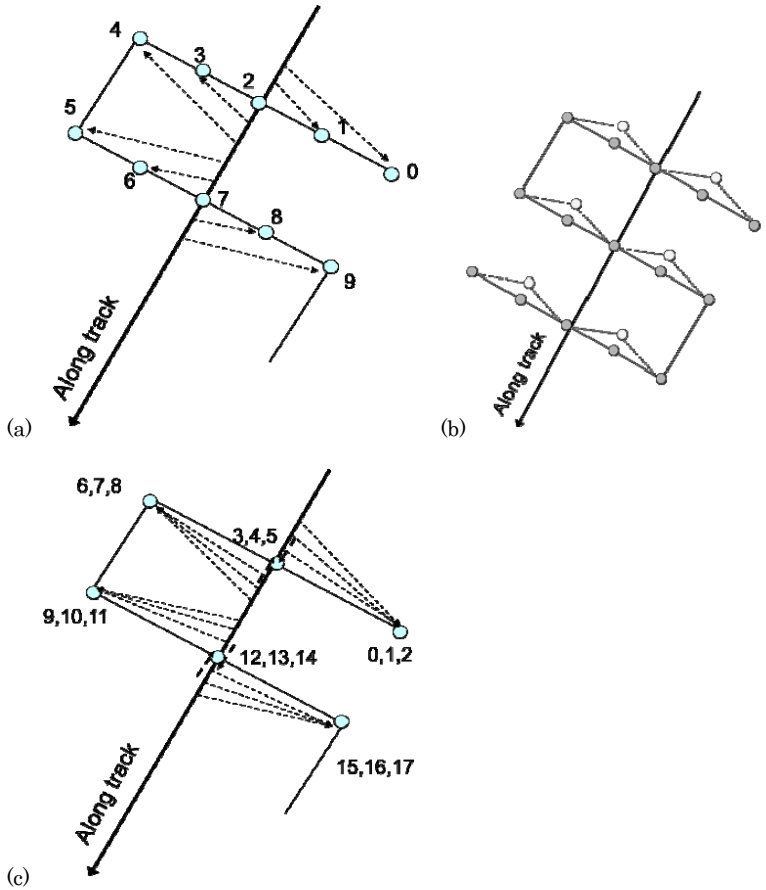

Fig. 2. Grid observation patterns: **(a)** 5-point cross-track scan mode **(b)** a M shape grid overwritten on 5-point cross-track scan mode, and **(c)** 3-point cross-track scan mode.

AMTD
5, 2959–3018, 2012

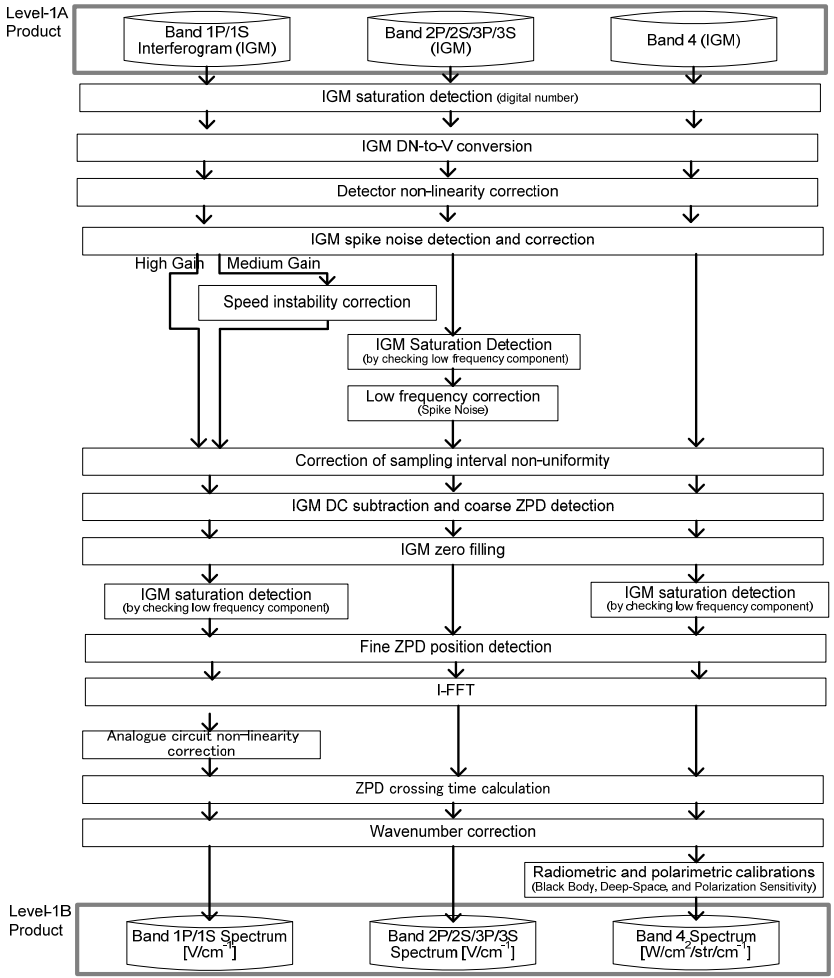

Fig. 3. The TANSO-FTS Level 1 data processing flow.

AMTD
5, 2959–3018, 2012

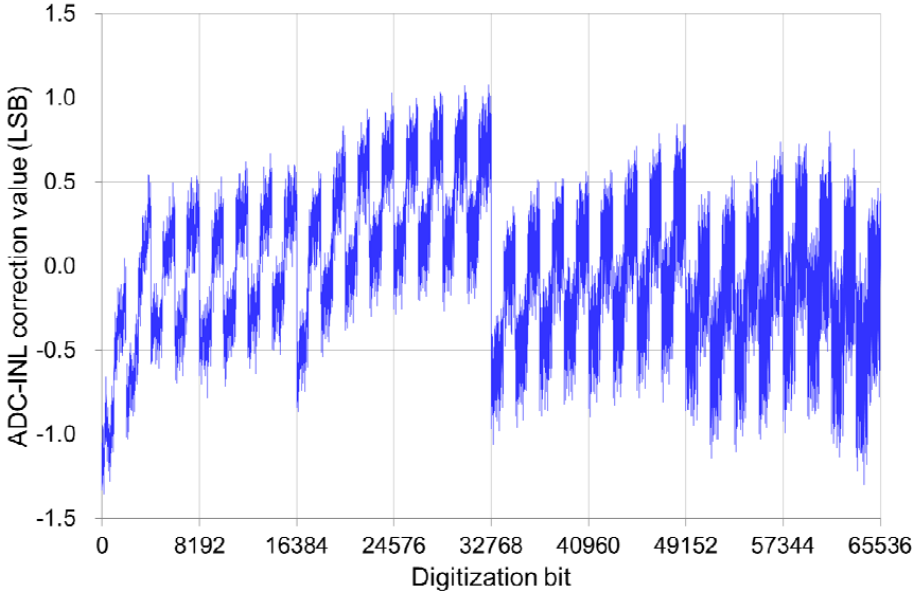

Fig. 4. ADC integral non-uniformity correction value retrieved from the measured data using the engineering model.

AMTD
5, 2959–3018, 2012

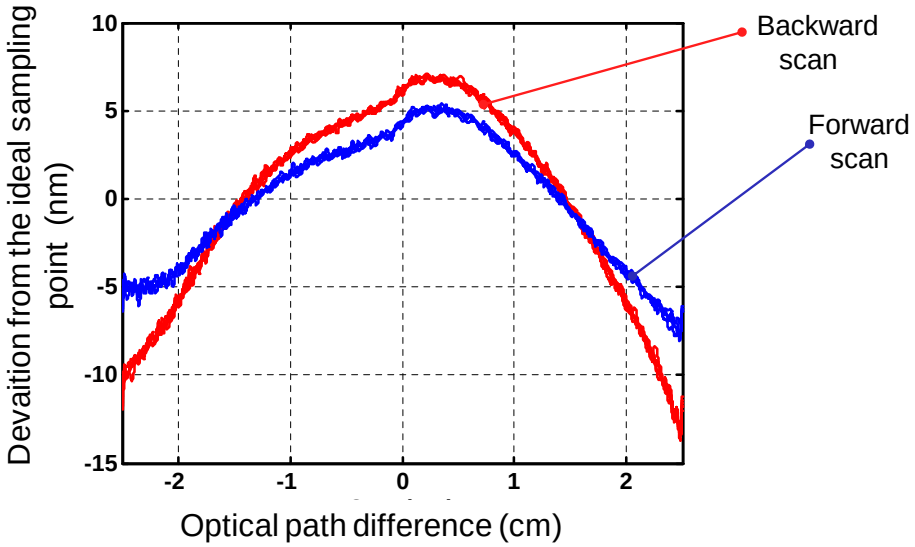

Fig. 5. Sampling interval non-uniformity as a function of OPD of the forward and backward scans.

AMTD
5, 2959–3018, 2012

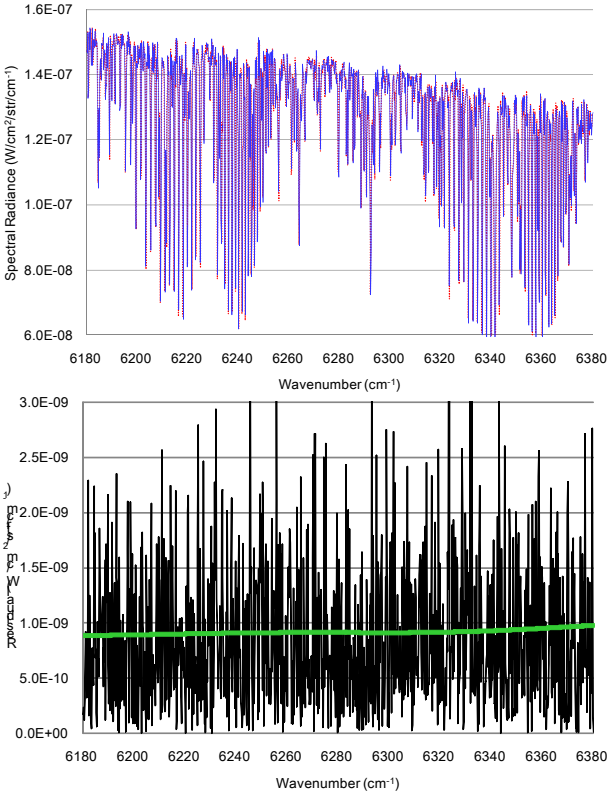

Fig. 6. (a) Measured CO_2 spectrum (blue solid line) of the Level 1B V050.050 along with the modeled spectrum for the retrieval (red dotted line) and **(b)** the residual difference (black solid line) together with the noise level (bold green line) (courtesy of Y. Yoshida of NIES).

AMTD
5, 2959–3018, 2012

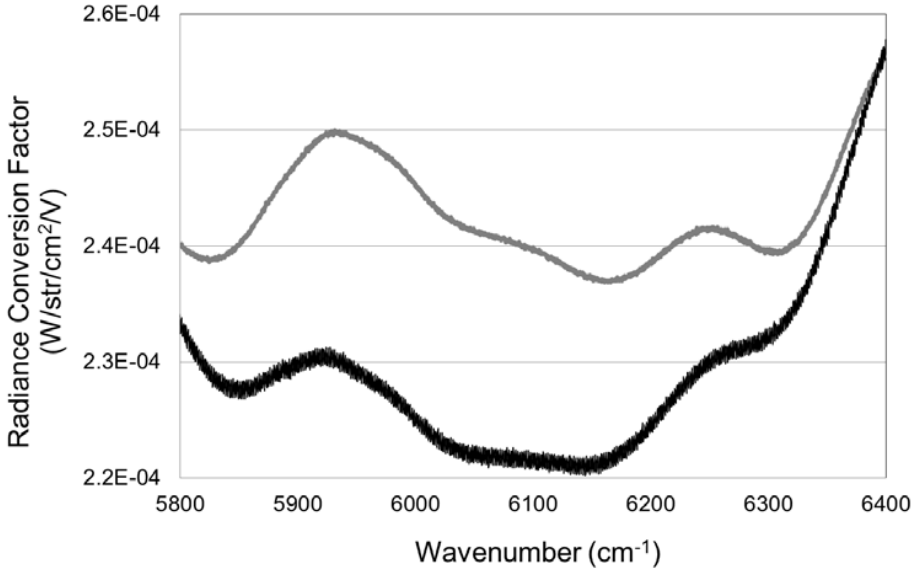

Fig. 7. Radiance conversion factors from the Level 1B data to the spectral radiance for the TANSO-FTS Band 2P (bold gray line) and 2S (solid line) of high gain.

AMTD
5, 2959–3018, 2012

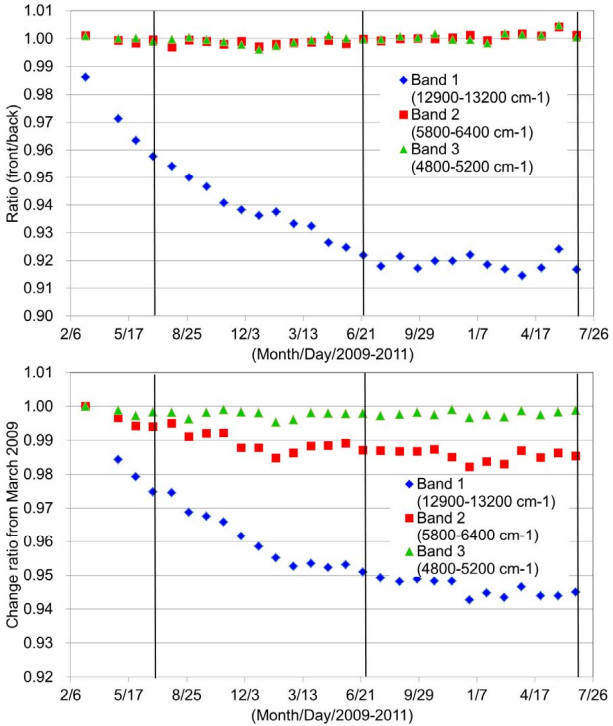

Fig. 8. Solar irradiance monthly calibration data from the onboard Spectralon diffuser, which indicates the change from the first measurement in space after correction for the distance between the satellite and the sun and the angle of incidence of the solar beam upon the diffuser. The vertical lines represent the time of the 2009, 2010 and 2011 vicarious campaigns: **(a)** ratio of the front side radiance to the back side one and **(b)** back side calibration.

AMTD
5, 2959–3018, 2012

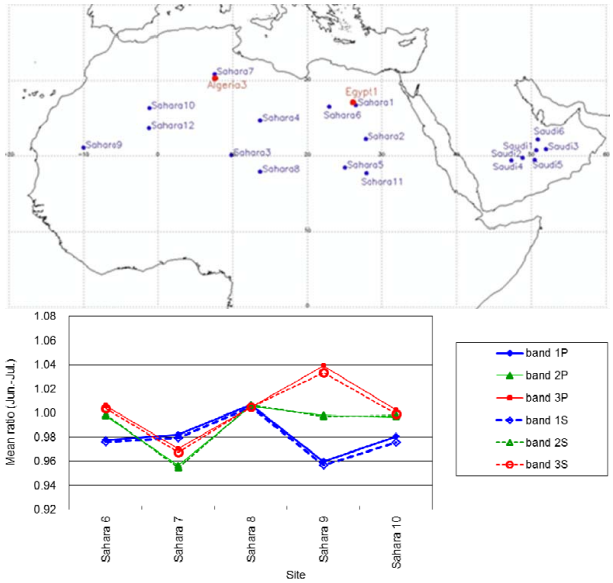

Fig. 9. (a) Radiance monitoring sites over the Sahara and Arabian deserts. **(b)** TANSO-FTS degradation in one year between 2009 and 2010 over the Sahara desert.

AMTD
5, 2959–3018, 2012

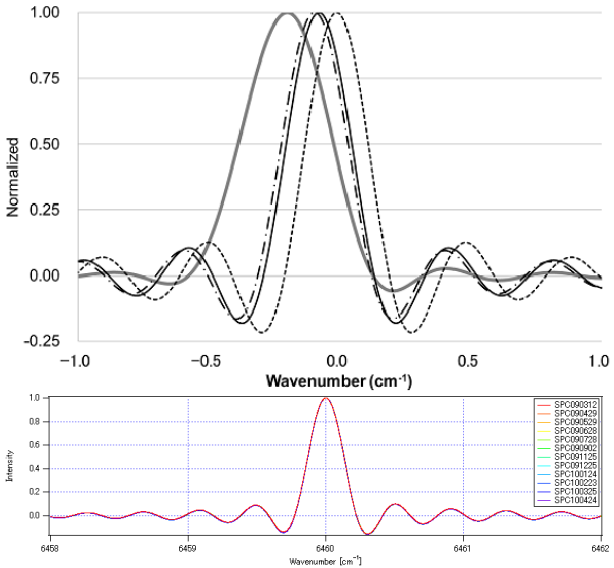

Fig. 10. (a) ILSF models at typical wavelength of each spectral band: 13050 cm-1 of Band 1P (bold gray), 6025 cm^{-1} of Band 2 (dash-dotted), 5000 cm^{-1} of Band 3 (solid) and 700 cm^{-1} of Band 4 (dotted). **(b)** Overwritten ILSF acquired monthly on orbit from March 2009 to April 2010 using the onboard diode laser.

AMTD
5, 2959–3018, 2012

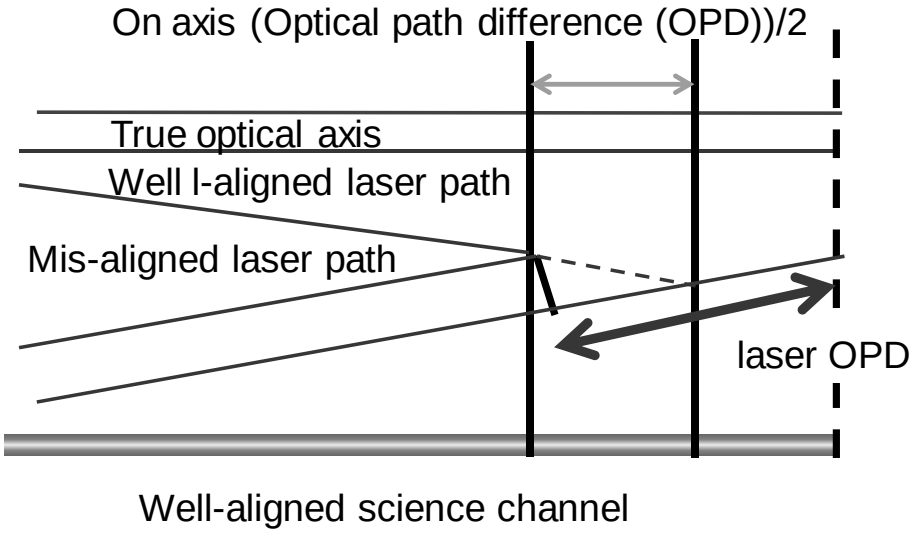

Fig. 11. Schematics of the sampling laser misalignment and OPD.

AMTD
5, 2959–3018, 2012

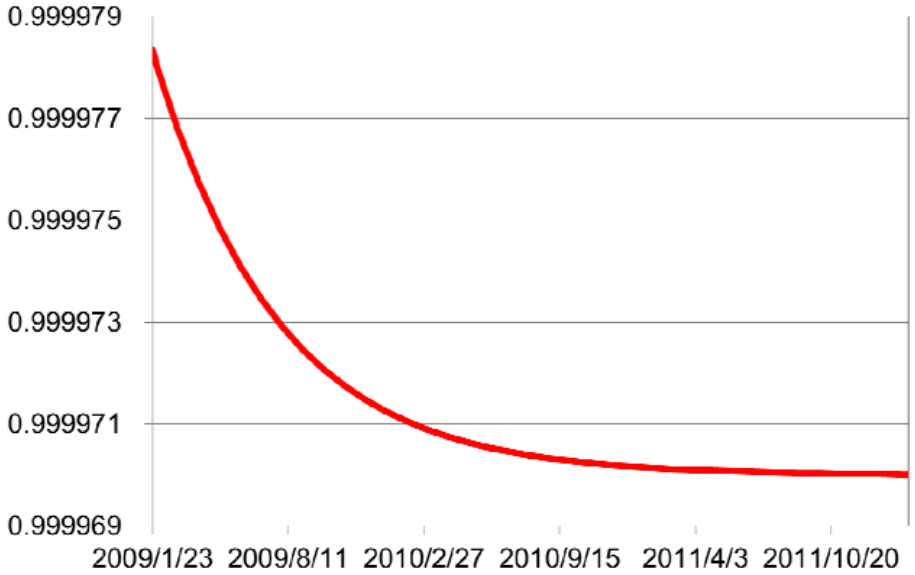

Fig. 12. Spectral calibration factor as a function of days from the launch.

AMTD
5, 2959–3018, 2012

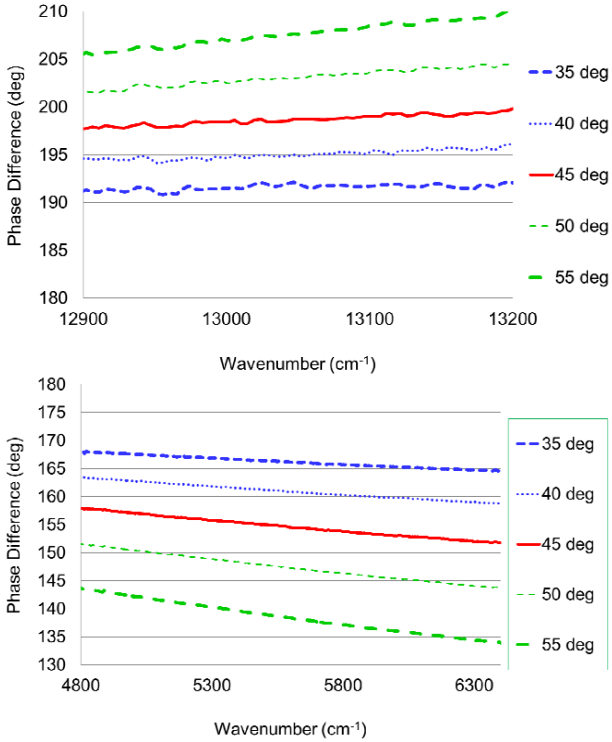

Fig. 13. Measured phase of the pointing mirror using the witness sample for Mueller matrix of incident angles of 35, 40, 45, 50 and 55 deg: **(a)** Band 1 and **(b)** bands 2 and 3.

AMTD
5, 2959–3018, 2012

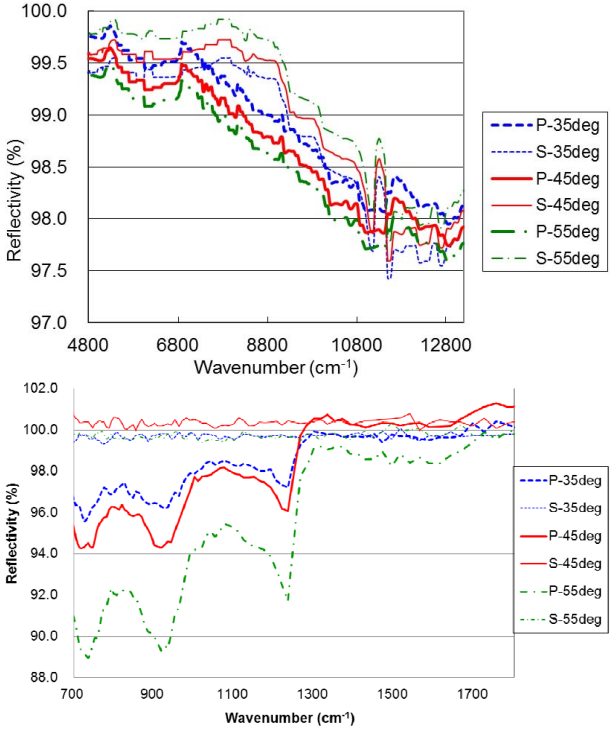

Fig. 14. Measured spectral reflectivity of the pointing mirror using the witness sample for two linear polarizations (P and S) of the incident angles of 35, 45, and 55 deg: **(a)** SWIR and **(b)** TIR.

AMTD
5, 2959–3018, 2012

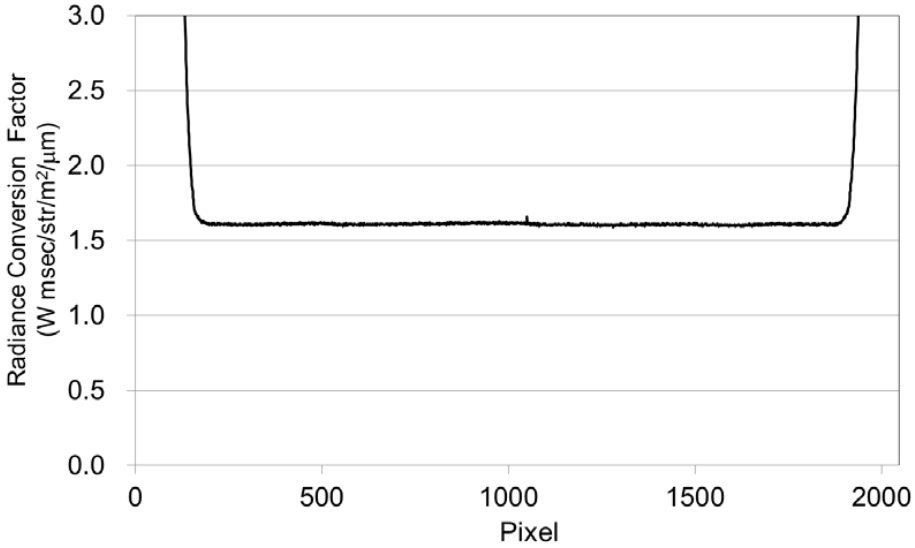

Fig. 15. Radiance conversion factors for the TANSO-CAI Band 1.

AMTD
5, 2959–3018, 2012

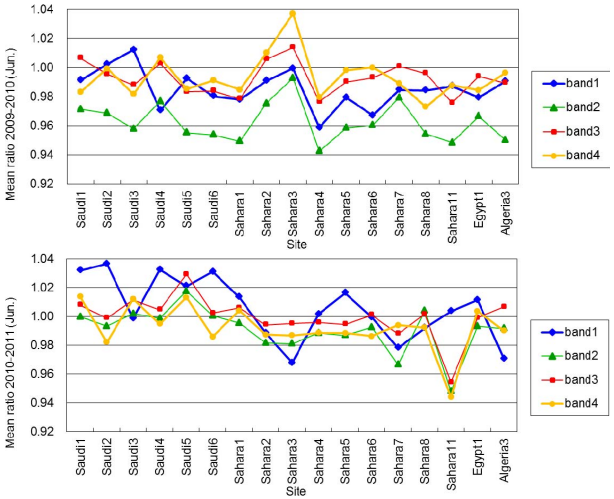

Fig. 16. (a) TANSO-CAI degradation in one year between 2009 and 2010 over the Sahara and Arabian deserts in June. **(b)** The same as **(a)** but for between 2010 and 2011.

AMTD
5, 2959–3018, 2012